

**NACA**

**UNCLASSIFIED**

TO: *TD 71-52 8-25-77*

# RESEARCH MEMORANDUM

for the

Atomic Energy Commission

AN INVESTIGATION OF THE AFTERBODY PRESSURE DISTRIBUTION

AND FIN LOADING CHARACTERISTICS OF A SPECIALIZED

STORE CONFIGURATION AT TRANSONIC SPEEDS

By Beverly Z. Henry, Jr., and John A. Braden

Langley Aeronautical Laboratory  
Langley Field, Va.

FF No. 602(A)	<b>X71 80119</b>	(THRU)
	(ACCESSION NUMBER)	<i>None</i>
	<i>54</i>	(CODE)
	(PAGES)	
	(NASA CR OR TMX OR AD NUMBER)	(CATEGORY)
	<b>Restriction/Classification Cancelled</b>	
	<b>ONLY</b>	

Declassified by authority of NASA  
Classification Change Notices No. *22-4*  
Dated \*\* *7-30-77*

## NATIONAL ADVISORY COMMITTEE FOR AERONAUTICS

WASHINGTON

1955

## NATIONAL ADVISORY COMMITTEE FOR AERONAUTICS

## RESEARCH MEMORANDUM

for the

Atomic Energy Commission

AN INVESTIGATION OF THE AFTERBODY PRESSURE DISTRIBUTION  
AND FIN LOADING CHARACTERISTICS OF A SPECIALIZED  
STORE CONFIGURATION AT TRANSONIC SPEEDS

By Beverly Z. Henry, Jr., and John A. Braden

## SUMMARY

An investigation was conducted in the Langley 8-foot transonic pressure tunnel to determine the afterbody pressure distribution and fin loading characteristics of two configurations of the TX-21 special weapon. The two configurations differed in nose contour only, with one having a hemispherical-flat shape and the other a double-radius ogive-flat shape. The tests were conducted in the Mach number range from 0.50 to 1.21. Reynolds number, based on body maximum diameter, varied from  $1.5 \times 10^6$  to  $2.3 \times 10^6$ .

The differences in nose contour caused no significant changes in the results obtained within the available range of comparison. The most favorable location for a pressure-sensing port was indicated to be at about the 89-percent-body station which gave a maximum equivalent altitude error of 2,600 feet for oscillatory motion confined to  $\pm 4^\circ$ .

Only small changes in fin loading characteristics were noted in the low angle-of-attack range ( $\alpha < 6^\circ$ ) whereas at the higher angles there was an outboard shift in loading. The combined effects of a high degree of flow acceleration over the forward portion of the body and the movement of the body shock waves subjected the fins to unique variations in local pressure in the Mach number range  $0.92 < M_0 < 1.07$ .

Lift-curve slope for the complete configuration was greater at angles of attack exceeding  $4^\circ$  than at angles of attack near zero. The configurations tested remained statically stable throughout the range of the investigation.


  
 INTRODUCTION

In recent years, considerable research effort has been devoted to the development of special aeroballistic body shapes, capable of being released from altitudes above 50,000 feet from aircraft operating at Mach numbers near unity. One of the major problems associated with the aerodynamic capabilities of these weapons under such release conditions has been that of longitudinal stability in the transonic and low supersonic speed ranges.

In accordance with a request from the Atomic Energy Commission and in cooperation with the Sandia Corporation, tests of the TX-21 special weapon have been conducted in the Langley 8-foot transonic pressure tunnel. The purpose of these tests was to define the effect of Mach number and angle of attack on the longitudinal stability characteristics of the weapon and to determine pressure distribution characteristics over the afterbody and stabilizing fins. It was further desirable to locate, if possible, a pressure port which would be relatively insensitive to Mach number for use in conjunction with a barometric fusing device.

The dynamic and static longitudinal stability characteristics of several TX-21 configurations have been reported in reference 1. The present report presents the results of pressure measurements made over the afterbody and fins of two TX-21 configurations which were similar but not identical to those of reference 1. Inasmuch as the results presented herein constitute only a component part of the special weapons program, a complete evaluation of the TX-21 is beyond the scope of this paper.

## SYMBOLS


A            area, sq ft

$C_m$         pitching-moment coefficient,  $\frac{\text{Pitching moment}}{q_0 A d}$

$C_N$         normal-force coefficient,  $\frac{\text{Normal force}}{q_0 A}$

$C_{A_f}$      fin axial-force coefficient,  $\sum P \left( \frac{\Delta A}{A} \right)$

$C_{m_f}$      fin pitching-moment coefficient,  $\sum P \left( \frac{\Delta A}{A} \right) \left( \frac{x}{c} \right)$

$C_{N_f}$	fin normal-force coefficient, $\sum P\left(\frac{\Delta A}{A}\right)$
$C_{m_\alpha}$	static longitudinal stability parameter, $\frac{\partial C_m}{\partial \alpha}$
L	body length, ft
$M_o$	free-stream Mach number
P	pressure coefficient, $\frac{P - P_o}{q_o}$
R	Reynolds number, based on d
b	fin span, ft
c	fin chord, ft
$C_{m_f}$	fin section pitching-moment coefficient, $\sum P\left(\frac{\Delta x}{c}\right)\left(\frac{x}{c}\right)$
$C_{N_f}$	fin section normal-force coefficient, $\sum P\left(\frac{\Delta x}{c}\right)$
d	maximum body diameter, ft
p	local static pressure, lb/sq ft
$P_o$	free-stream static pressure, lb/sq ft
$q_o$	free-stream dynamic pressure, lb/sq ft
x	chordwise distance, ft
y	spanwise distance, ft
$\alpha$	angle of attack, deg

## APPARATUS AND MODELS

## Wind Tunnel

This investigation was conducted in the Langley 8-foot transonic pressure tunnel which has a slotted test section and permitted continuous testing to a Mach number of about 1.2 for these models. Details of the

tunnel test section are given in reference 2. Tunnel calibrations have indicated that the maximum deviation from the average free-stream Mach number is about  $\pm 0.004$  at subsonic speeds and about  $\pm 0.008$  at Mach numbers above 1.00.

### Models

Two TX-21 configuration models were tested in the investigation. The configurations were similar with the exception of the nose contour. (See fig. 1.) These models, provided by the Sandia Corporation, consisted of either a hemispherical-flat nose, designated herein as nose A, or a double-radius ogive-flat nose, designated herein as nose B, attached to a 6.5-inch-diameter cylindrical afterbody. Cylindrical extensions were interposed between the nose and afterbody sections to maintain an approximately constant model length. The configuration with nose A was 16.756 inches long whereas that with nose B was 16.779 inches long. The fineness ratio of either configuration was 2.58.

The bodies were constructed of aluminum and brass and were instrumented with three rows of static-pressure orifices as shown in table I. Stabilizing fins and other accessory parts (fig. 1) were screw fastened to the bodies.

Details of the fins and other model accessories are given in figures 1(b) and 1(c). Although the locations of the model accessories differed slightly for the two configurations (fig. 1), the accessory parts used (i.e., fins, spoiler bands, spoiler flange, and nut covers) were the same for both models. The cruciform fin configuration consisted of two diametrically opposed brass pressure fins and two aluminum fins (fig. 1(b)). The shape of the aluminum fins corresponded closely to the actual fin on the TX-21 prototype whereas the pressure fins were modified to facilitate the installation of static-pressure orifices. The pressure fins differed from the actual fins in that they had a slightly larger span and were not raked at the beginning of the second wedge. The pressure fins contained 45 static-pressure orifices located as shown in figure 1(b) on one surface only and 5 static-pressure orifices on the fin base.

### TESTS AND METHODS

The models were installed in the test section with the nose flat at about the 106-inch tunnel station. A sketch of a typical configuration mounted on the tunnel support system is shown in figure 2. The model was positioned on the support system with the chord plane of the pressure fins in a horizontal position. In this position the planes of the body

orifice rows were as shown in table I. In order to determine fin loads, it was necessary to test the models at both positive and negative angles of attack since pressure measurements were obtained only on one side of the fins.

Data were obtained on the nose A configuration through a Mach number range from 0.50 to 1.16 at angles of attack from  $-10^{\circ}$  to  $+10^{\circ}$  in  $2^{\circ}$  increments. The complete angle-of-attack range ( $\alpha = \pm 10^{\circ}$ ) was not obtained at all test Mach numbers. The nose B configuration was tested through the Mach number range from 0.50 to 1.21 at  $-2^{\circ}$ ,  $0^{\circ}$ , and  $+2^{\circ}$  for all test Mach numbers. The test Reynolds number, based on maximum body diameter, varied from about  $1.5 \times 10^6$  to about  $2.3 \times 10^6$ . (See fig. 3.)

All pressure data were photographically recorded from multitube manometers. Tunnel total pressures were manually recorded from an automatically indicating mercury-filled barometer. Visual observation of the flow in the vicinity of the model was obtained by standard schlieren photography.

#### REDUCTION OF DATA

The pressure measurements made over the model afterbody were directed toward the evaluation of the pressure-sensing characteristics of the individual orifices. Results of these measurements are therefore presented as the variation of the pressure ratio  $p/p_0$  with Mach number. Since no measurements were obtained of the pressures over the model noses, these data are inadequate for the calculation of body forces.

Three component forces on the fins were obtained from pressure measurements. In the reduction of these data, a numerical summation method was employed to obtain values of normal force, pitching moment, and axial force. In this method, the pressure acting at any orifice was assumed to act on the area from the orifice to a boundary midway between the orifice in question and the adjacent orifices. Summation of these pressure-area increments then provided a total-force value. Since the fins were instrumented on the upper surface only, the values shown for the lower surface were obtained by testing at negative angles of attack. Values presented are based on the exposed area of a single fin and on the fin chord. Pitching-moment values were taken about the fin leading edge.

Normal-force and pitching-moment data for the complete configurations were obtained from the output of two sets of calibrated strain gages mounted on the pressure-model sting support. No strain-gage measurements of axial force were obtained. The results presented are based on body frontal area and body maximum diameter.

  
ACCURACY

As discussed in reference 1, the body flow fields were influenced in the Mach number region from about 1.08 to 1.14 by a reflection of the model bow wave from the tunnel wall. Results obtained in this Mach number region would contain spurious results in comparison to results in free air. It would be expected that, at Mach numbers somewhat higher than 1.14, the effect of this reflected disturbance would be felt over the model base because of the upstream propagation through the wake.

The accuracy of the pressure ratio  $p/p_0$  and angle of attack  $\alpha$  is considered to be within  $\pm 0.002$  and  $\pm 0.1^\circ$ , respectively. The accuracy of the pressure coefficient  $P$  is considered to be  $\pm 0.005$ .

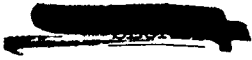
The values of fin axial force presented are possibly in error by an undetermined amount because of the small number of orifices available to determine the force contribution of the fin base (fig. 1(b)).

No attempt has been made to present the limits of accuracy for the force measurements inasmuch as installation of the strain gages on the model sting was incorporated in these pressure tests to provide only general trends and approximate levels of normal force and pitching moment. It is felt that the accuracy of the values obtained is adequate for these purposes.

## RESULTS AND DISCUSSION

An investigation was made of two TX-21 configurations to determine the afterbody pressure distribution and fin loading characteristics. The first configuration employed a hemispherical-flat nose, nose A, and was tested through the angle-of-attack range from  $0^\circ$  to  $10^\circ$  while the second configuration employed a two-radius ogive-flat nose, nose B, and was tested at  $0^\circ$  and  $2^\circ$ . Consequently, comparisons are available in only a limited angle-of-attack range. No significant differences in the results obtained for the two configurations were noted in this range. Therefore, in the discussion which follows, no distinction will be made between the two configurations except where noted.

The character of the model flow fields were qualitatively similar for the configurations tested. A general depiction of these flow fields was presented in reference 1, wherein it was noted that compression waves originating from the forward portion of the nose and from spoiler bands formed at Mach number as low as about 0.75. These disturbances terminated in a normal shock which moved rearward with increases in Mach number reaching the fin leading edge at  $M_0 \approx 0.94$ . Accelerations of the flow



around the body as indicated by changes in local Mach number increased with stream Mach number reaching a maximum at a stream Mach number of about 0.99 and diminished at higher speeds. The combined effects of this high degree of flow acceleration and the movement of the body shock waves exposed the fin surfaces to unique variations in local pressure in the range  $0.92 < M_o < 1.07$ . This will be discussed in greater detail in the section entitled "Fin Loads." In all cases the boundary layer surrounding the body remained quite thick and acted as an attenuating influence which tended to diffuse sharp discontinuities.


### Pressure Port

A satisfactory pressure-sensing port which could be incorporated in a barometric fusing device for arming these weapons at specified altitudes should maintain the ratio of local to ambient static pressure as near unity as possible. In order to evaluate this characteristic of the body pressure ports investigated on the TX-21 configurations, the data have been presented in figures 4 and 5 as the variation of the static pressure ratio  $p/p_o$  with Mach number for each longitudinal orifice location. The location of these orifices may be found in table I and are given in the figures as the distance from the nose flat in percentage of body length. Included in each figure is a scale of equivalent altitude error for which a fusing altitude of 3,000 feet was arbitrarily selected. It will be noted from these figures that the two orifice rows labeled side and bottom give essentially identical readings. This results from the model being so oriented as to place the pressure fins in the horizontal plane with the consequent similar location of the two rows with respect to the angle-of-attack plane (table I).

An examination of figures 4 and 5 indicates that the most favorable location for a pressure-sensing port will be in the vicinity of stations 0.893 to 0.938. At  $0^\circ$  angle of attack the maximum altitude error at these stations is about 1,300 feet. A maximum error of 4,400 feet is noted at an angle of attack of  $10^\circ$ . If the limits of oscillation are confined to  $\pm 4^\circ$ , however, the maximum error indicated is 2,600 feet. With the oscillatory motion confined to  $\pm 4^\circ$ , station 0.893 appears to be slightly superior to station 0.938.

The values discussed in the preceding paragraph have been taken with any existing tunnel effects, such as the wall-reflected bow wave, included. The one exception to this statement lies in the ignoring of the apparently erroneous data shown for the nose A configuration at  $\alpha = 2^\circ$  and  $M = 1.077$ . It is believed that correction of these results to a free-air condition would tend to reduce the errors noted. No attempt has been made to apply such a correction because of the unknown magnitude of the effect.



  
Fin Loads


Presented in figures 6 to 10 are the results of measurements made to determine the fin loads. In figures 6 and 7 are shown the pressure distributions over the fins for the configurations with nose A and nose B, respectively. Values of section normal-force coefficient and section pitching-moment coefficient for the nose A configuration are shown in figures 8 and 9, respectively. Values of total fin normal-force coefficient, pitching-moment coefficient, and axial-force coefficient are given in figure 10. It will be noted in these figures that, with the exception of axial-force coefficient in figure 10, no  $0^\circ$  angle-of-attack results have been presented since, owing to the method of testing and computation, these values would be zero.

An examination of the fin surface pressure distributions (figs. 6 and 7) shows no significant variation as Mach number is increased. Over the inboard portions of the fin, most of the load appears to be carried near the leading edge. The loading on the outboard portions of the fin is similar to that of the inboard portion at angles of attack below about  $6^\circ$ . At higher angles of attack, a rearward shift in loading of the outboard portion can be seen. At Mach numbers above about 0.90, the rearward shift in loading appears to be felt somewhat farther inboard from the fin tip.

Values of section normal-force coefficient presented in figure 8 indicate that the spanwise load distribution is similar for all Mach numbers. At angles of attack below  $6^\circ$ , the spanwise loading remains essentially constant to approximately midspan. Outboard of this point, the loading decreases toward the tip. At angles of attack above  $6^\circ$ , the loading shifted well outboard. The trends of section pitching-moment coefficient shown in figure 9 follow very closely those noted for section normal-force coefficient.

In table II are tabulated the values of spanwise center-of-pressure location. It can be seen from these values that the fin center of pressure moves outboard as angle of attack is increased for all Mach numbers investigated. The maximum movement of about 7 percent was observed at a Mach number of 0.918. This outboard shift in loading may be associated with the emergence of the outboard portions of the fins from the very thick boundary layer surrounding the body.

The variations of total fin forces with Mach number are presented in figure 10 for several angles of attack. The normal-force coefficient increases with angle of attack at all Mach numbers. The magnitude of the increase is greater at the higher speeds. Normal-force coefficient increases with Mach number to a Mach number of about 0.92, above which there is a leveling off at a value slightly lower than that observed at  $M_0 = 0.918$ . Variations in pitching-moment coefficient shown in the same figure follow very closely those noted for normal-force coefficient.




Values of chordwise center-of-pressure location tabulated in table II indicate that the center-of-pressure movement is similar at all speeds. As the angle of attack is increased to  $6^\circ$ , there is a forward movement of the center of pressure. Increasing angle of attack above  $6^\circ$  results in a rearward shift. The overall movement is relatively small and covers only about 14 percent of the chord. The maximum movement of about 9 percent of the chord was observed at a Mach number of 1.157. This small movement appears to result from the restricted nature of the boundary layer which covers such a large portion of the fin span.

The variation of fin axial-force coefficient with Mach number at several angles of attack is shown in figure 10(b). The axial force increases normally at subsonic speeds until a Mach number of about 0.92 is reached. As Mach number is further increased, a sudden reduction in axial force occurs reaching a minimum value at  $M_0 \approx 0.98$ . Above  $M_0 \approx 0.98$ , the axial force rises to a normal level except at  $M_0 \approx 1.15$  where the interference of the reflected model bow wave causes a force reduction.

The unusual reduction in fin axial force noted in the range  $0.92 < M_0 < 1.07$  is believed to be due to a unique fin environmental condition and would not be apparent in force measurements of the complete configuration which are not available. Calculations of local Mach number from body surface pressures in the vicinity of the fins indicate that, at free-stream Mach numbers below about 0.92, local Mach number is very close to free-stream Mach number. Above  $M_0 \approx 0.92$ , local Mach number is increasingly greater than free-stream Mach number reaching a maximum deviation at  $M_0 \approx 1.00$ . Above  $M_0 \approx 1.00$ , this deviation is greatly reduced. These changes in local Mach number are indicative of local flow accelerations over the body.

At free-stream Mach numbers below about 0.94, the body normal shock is ahead of the fin leading edge and effectively shields the fin surface from the negative pressure field induced by the local flow acceleration. An examination of the relative contributions of the fin surface and base to total fin axial force indicates that this shock reaches the fin base at  $M_0 \approx 0.96$  as evidenced by a minimum point in fin-base force. This rearward movement of the shock exposes the fin surface to the negative pressure field with a resulting forward component which continues to increase to a free-stream Mach number of about 1.00. Above  $M_0 \approx 1.00$ , the normal shock no longer exists on the body and the flow acceleration decreases with a resulting increase in fin axial force to what may be considered a normal level.

  
Force Measurements

Results of force measurements made in conjunction with the pressure tests to determine normal-force and pitching-moment coefficients are shown for the nose A and nose B configurations in figures 11 and 12, respectively. Pitching-moment calculations were made relative to the 40.3-percent-body station for the nose A configuration and the 40.4-percent-body station for the nose B configuration.

The variation of normal-force coefficient with angle of attack was similar for Mach numbers below about 0.85. Increasing Mach number to 0.918 resulted in a rapid increase in lift-curve slope followed by a leveling off at higher speeds at values only slightly greater than those at subsonic speeds. It will be noted in figure 11 that, at angles of attack above about  $4^\circ$ , the lift-curve slope was greater than for the angles of attack near zero.


Pitching-moment-coefficient variations were similar to those noted for normal-force coefficient. In the range of the investigation, both configurations remained statically stable. Presented in figure 13 is a comparison between the static stability parameter  $C_{m_\alpha}$  obtained from force measurements and that obtained from the dynamic tests of reference 1. The agreement between the two curves is good. The differences noted, particularly at the higher Mach numbers, may be attributable to differences in fin orientation for the static tests (horizontal and vertical) and the dynamic tests ( $45^\circ$  from the horizontal) or to slight differences in configuration previously noted.

The center of pressure for these configurations moved rearward as Mach number was increased to about 0.92. There was a forward movement in the range  $0.92 < M_0 < 1.00$ . At Mach numbers greater than 1.00, the center-of-pressure location remained essentially constant at a position somewhat rearward of that noted for the subsonic case.

## CONCLUDING REMARKS

From an investigation of the afterbody pressure distribution and fin loading characteristics of two configurations of the TX-21 special weapon the following observations are made:

1. The most favorable location for a pressure-sensing port was indicated to be in the vicinity of the 89-percent-body station. If the oscillatory motion of the body is confined to  $\pm 4^\circ$ , the equivalent altitude error for this location was about 2,600 feet.




2. Only small changes in fin loading characteristics were noted at angles of attack below  $6^\circ$  as a result of the thick body boundary layer. At higher angles of attack, the outboard loading increased as the outboard portions of the fins apparently emerged from the body boundary layer.

3. The combined effects of a high degree of flow acceleration over the forward portion of the body and movement of the body shock waves subjected the fins to unique variations in local pressure in the Mach number range  $0.92 < M_0 < 1.07$ . This unique flow condition was evidenced by an unusual reduction in fin axial force in this Mach number range.

4. Normal-force coefficient for the complete configurations increased with angle of attack at all speeds. The lift-curve slope was greater at angles of attack exceeding  $4^\circ$  than at angles of attack near zero.

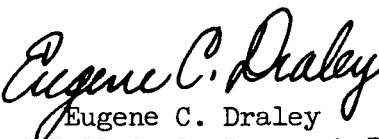
5. The two configurations tested remained statically stable throughout the range of the investigation. Comparison of these results with those obtained from dynamic tests of similar but not identical configurations showed good agreement.

Langley Aeronautical Laboratory,  
National Advisory Committee for Aeronautics,  
Langley Field, Va., July 16, 1956.

  
Beverly Z. Henry, Jr.  
Aeronautical Research Scientist

John A. Braden  
Aeronautical Research Scientist

Approved:

  
Eugene C. Draley

Chief of Full-Scale Research Division

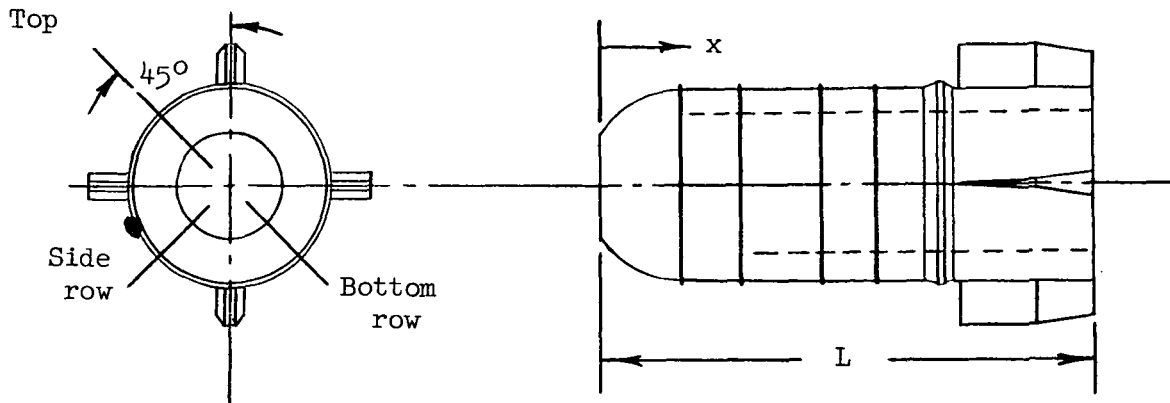
mhg

#### REFERENCES

1. Braden, John A.: An Investigation of the Longitudinal Stability Characteristics of Three Specialized Store Configurations at Transonic Speeds. NACA RM SL54L14, 1955.
2. Braden, John A., and Henry, Beverly Z., Jr.: An Investigation of the Longitudinal Stability and Afterbody Pressure Characteristics of Specialized Store Configurations at Transonic Speeds. NACA RM SL54C24, 1954.

TABLE I

## LOCATION OF BODY PRESSURE ORIFICES

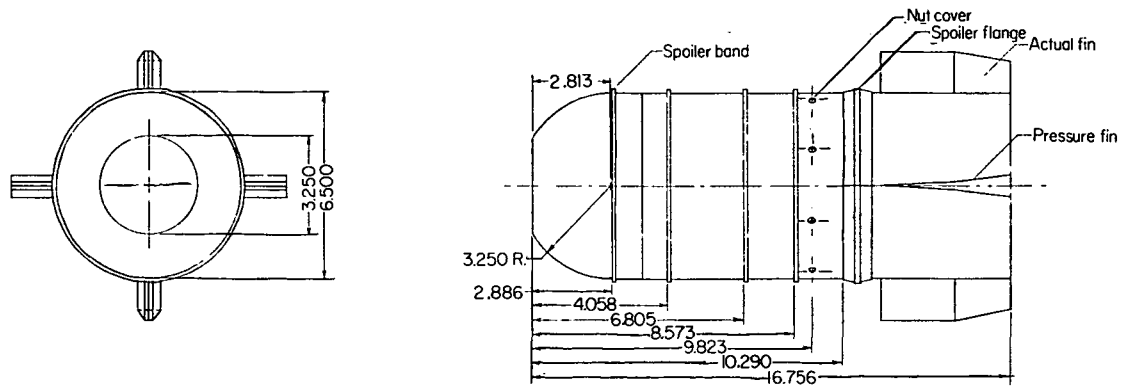


Orifice number			Nose A, L = 16.756 in.		Nose B, L = 16.779 in.	
Top	Side	Bottom	x, in.	x/L	x, in.	x/L
1			4.786	0.286	4.809	0.287
2			5.917	.353	5.940	.354
3	17	31	6.671	.398	6.694	.399
4	18	32	7.425	.443	7.448	.444
5	19	33	8.179	.488	8.202	.489
6	20	34	8.933	.533	8.956	.534
7	21	35	9.687	.578	9.710	.579
10	24	38	11.949	.713	11.972	.714
11	25	39	12.703	.758	12.726	.758
12	26	40	13.457	.803	13.480	.803
13	27	41	14.211	.848	14.234	.848
14	28	42	14.965	.893	14.988	.893
15	29	43	15.719	.938	15.742	.938
16	30	44	16.473	.983	16.496	.983

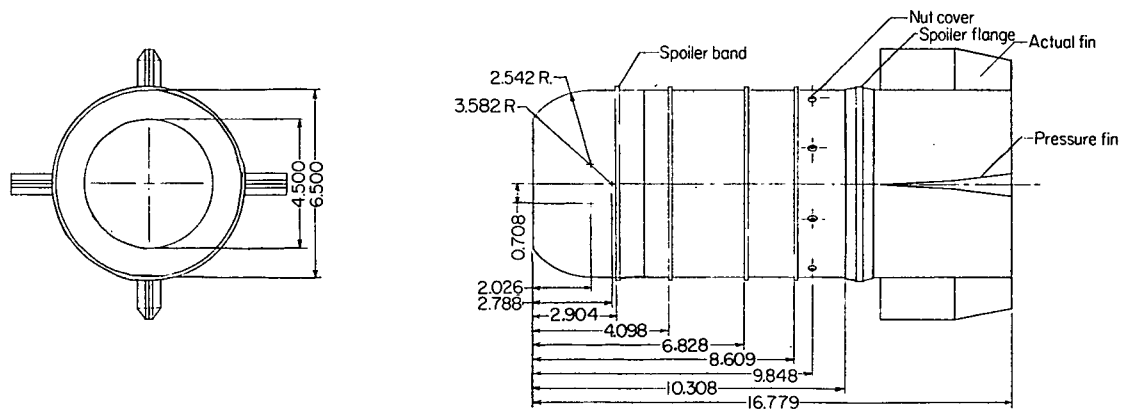
TABLE II

FIN CENTER-OF-PRESSURE LOCATION FOR  
NOSE A CONFIGURATION

Mach number	Angle of attack, deg	Chordwise location, x/c	Spanwise location, y/b
0.504	2	0.316	0.466
	4	.279	.471
	6	.258	.478
	8	.270	.504
	10	.323	.530
.801	2	.319	.465
	4	.307	.485
	6	.279	.494
	8	.303	.516
	10	.322	.531
.918	2	.332	.458
	4	.303	.489
	6	.301	.506
	8	.328	.525
	10	.356	.532
.993	2	.311	.466
	4	.302	.487
	6	.303	.487
	8	.341	.511
	10	.376	.527
1.077	2	.315	.478
	4	.303	.478
	6	.294	.480
	8	.339	.510
	10	.383	.528
1.157	2	.310	.483
	4	.302	.472
	6	.301	.485
	8	.341	.527
	10	.393	.533



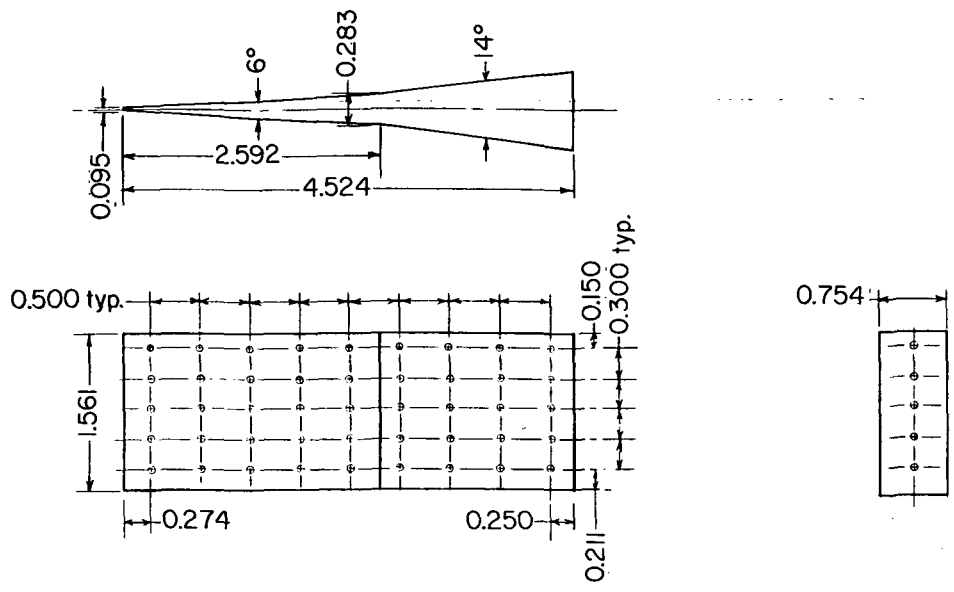
TX-21 with hemispherical-flat nose



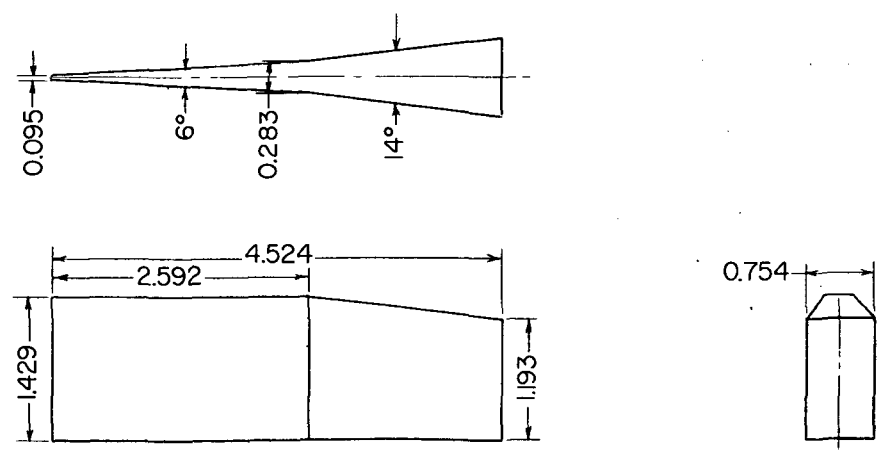
TX-21 with double-radius flat nose

(a) Model details.

Figure 1.- Details of the TX-21 test configurations. All dimensions are in inches.



Pressure fin

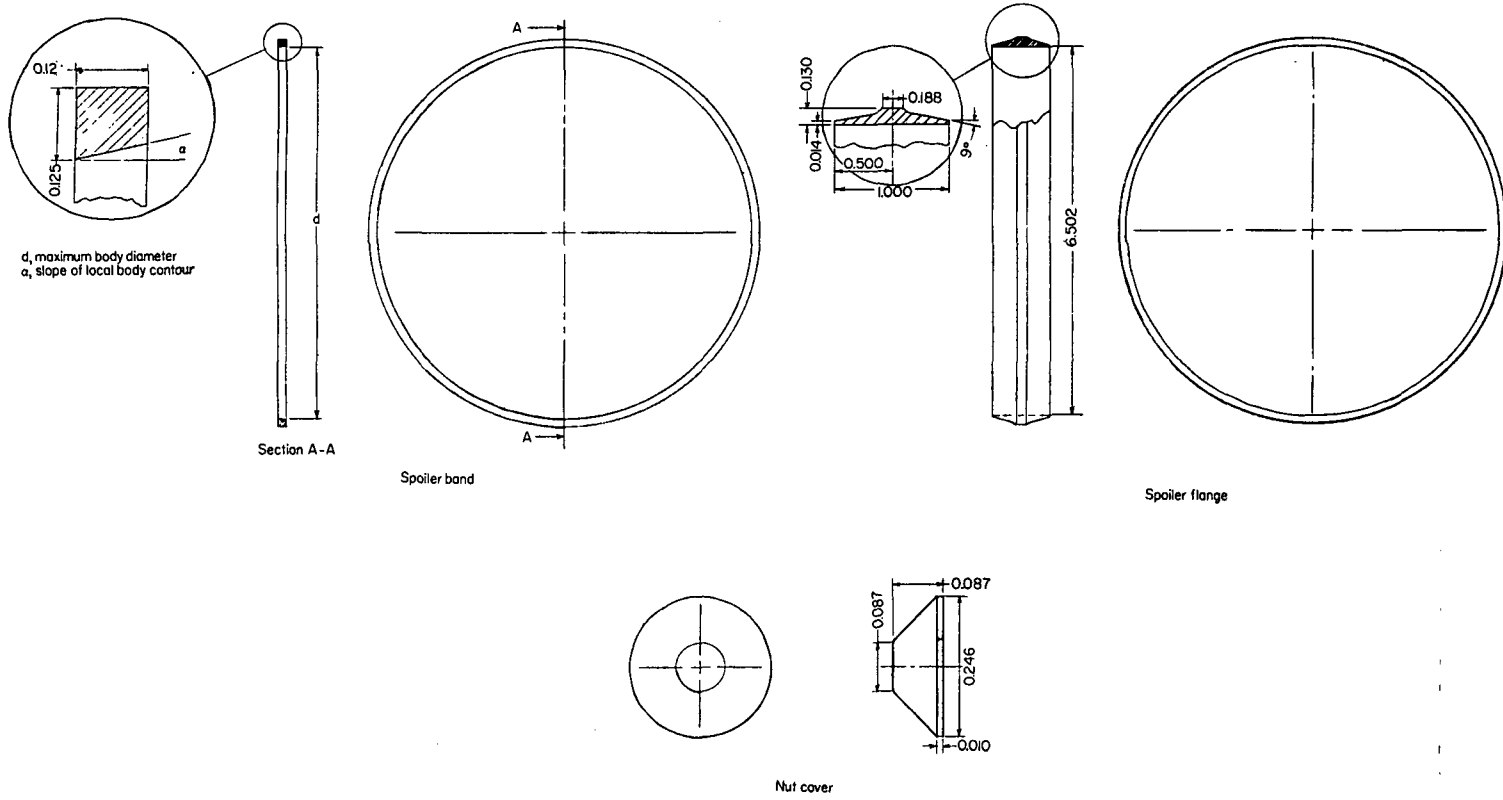


Actual fin

(b) Details of fins used with the test configurations.

Figure 1.- Continued.





(c) Details of accessory parts used with the test configurations.

Figure 1.- Concluded.

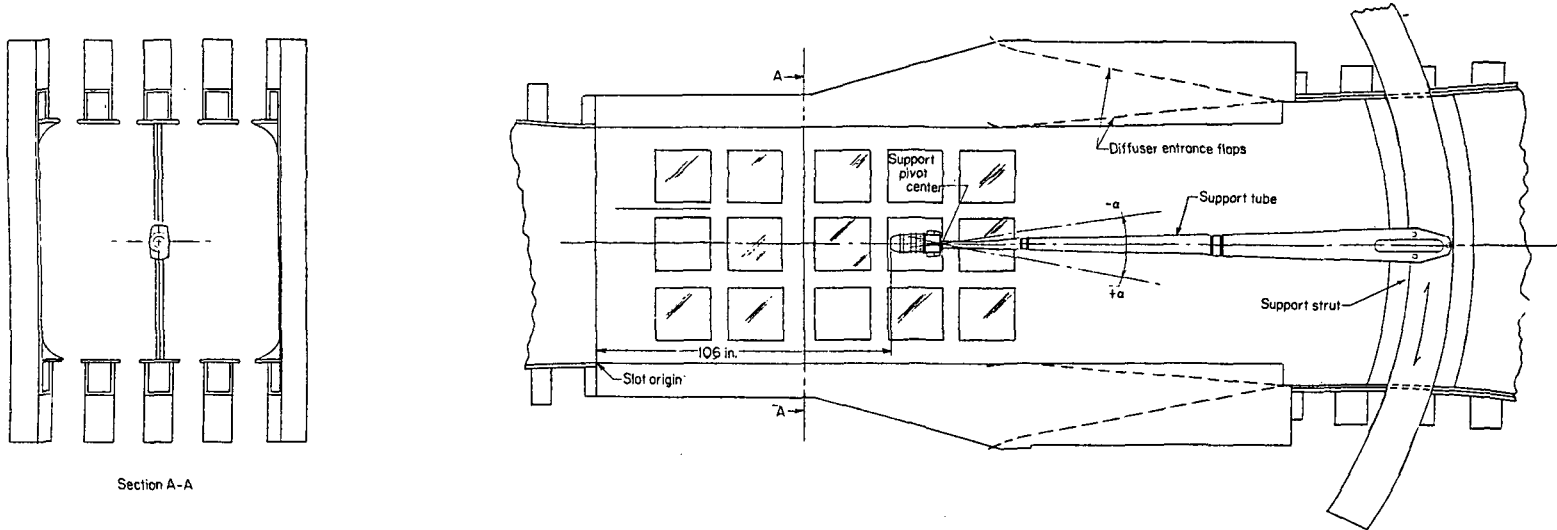


Figure 2.- General arrangement of a typical model installation in the Langley 8-foot transonic pressure tunnel. All dimensions are in inches.

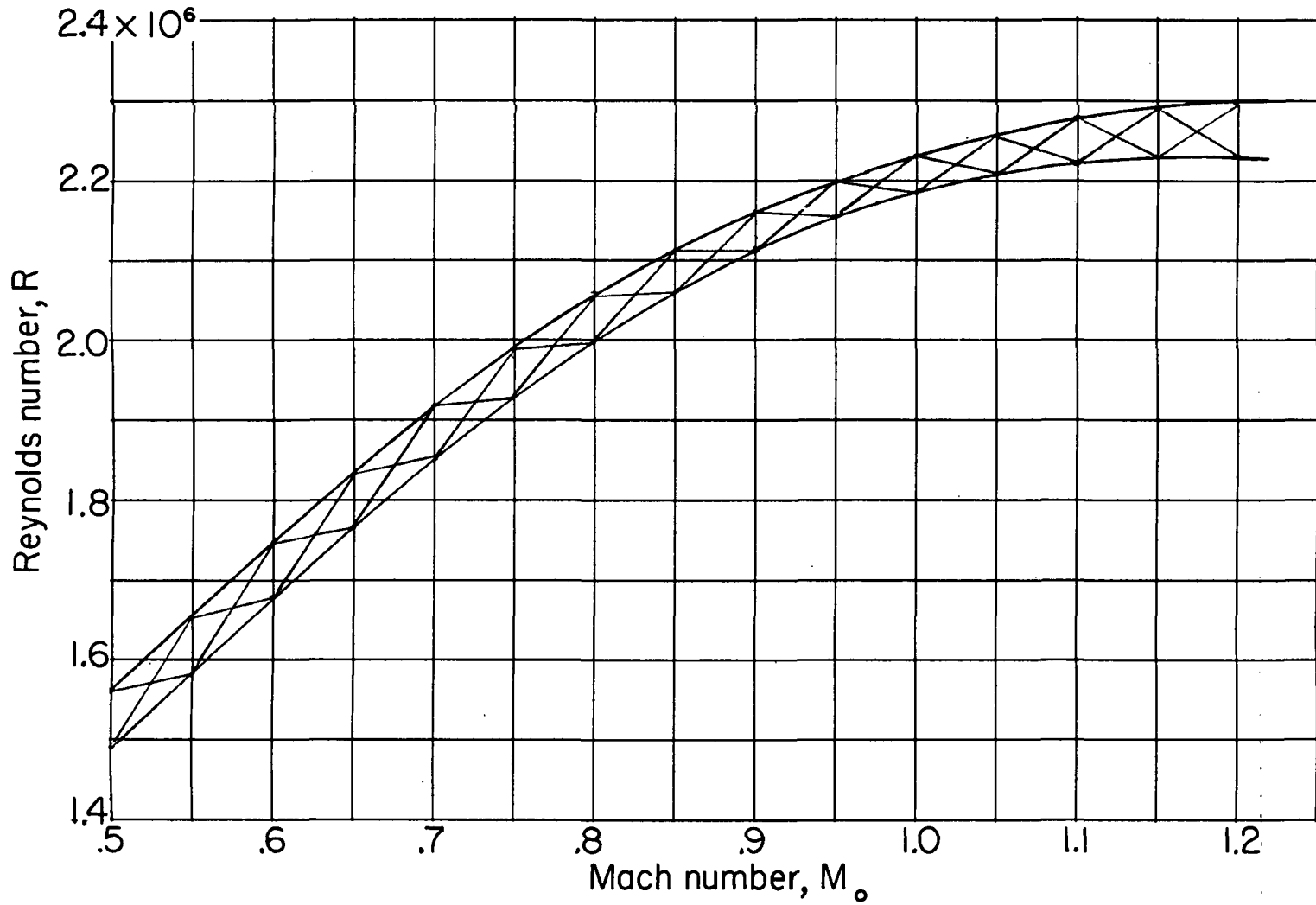
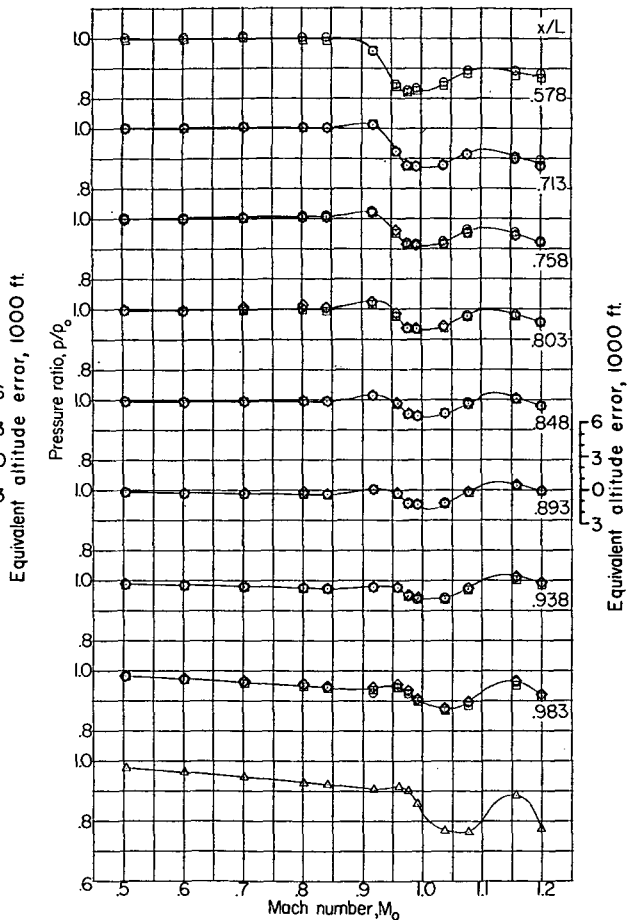
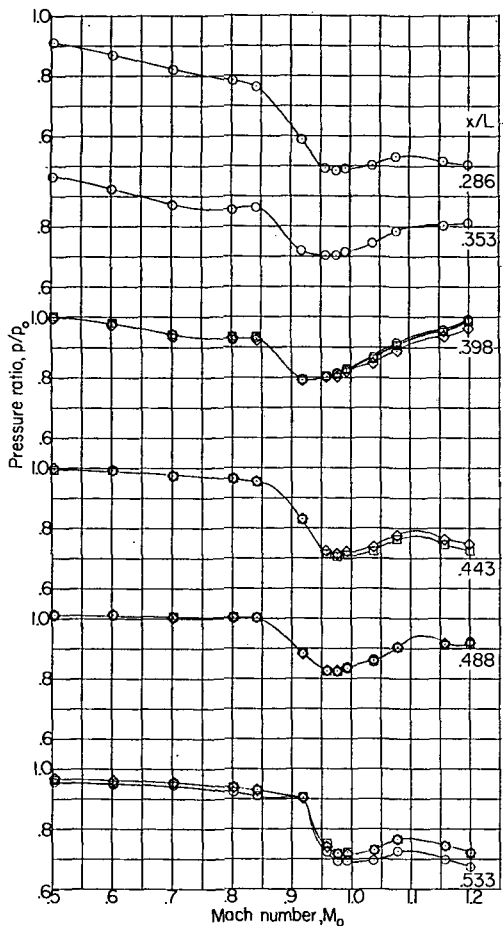


Figure 3.- Variation of Reynolds number based on a maximum body diameter of 6.5 inches.

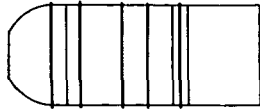


- Top row
- Side row
- ◇ Bottom row
- △ Base pressure

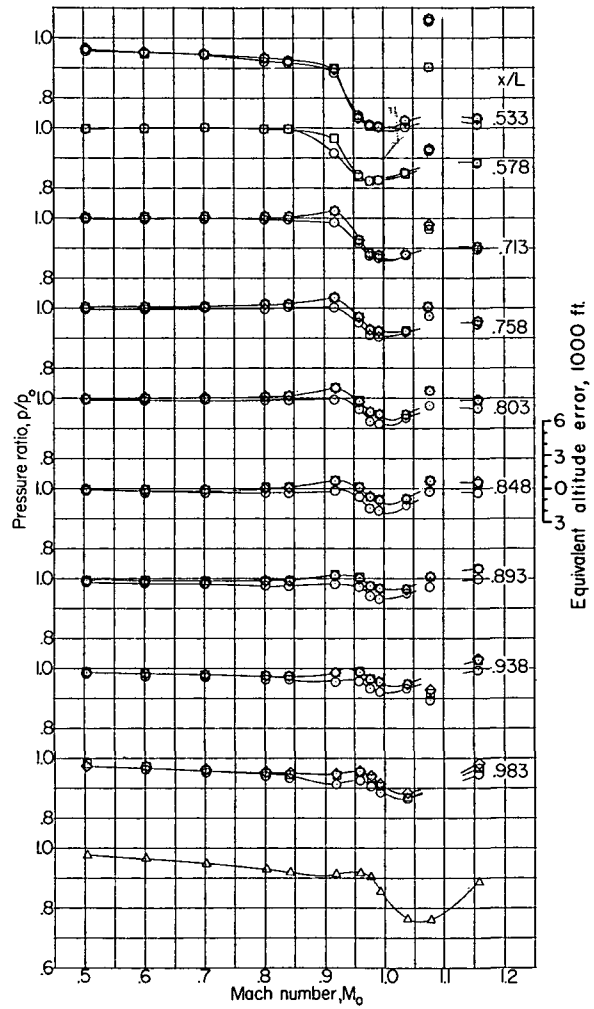
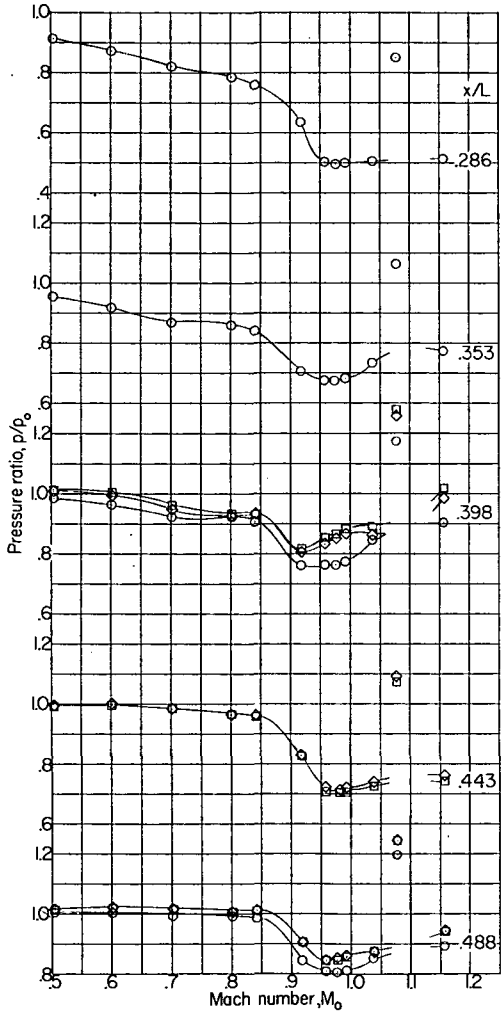


(a)  $\alpha = 0^\circ$ .

Figure 4.- The effect of Mach number and angle of attack on local static-pressure ratios over the TX-21, nose A, configuration afterbody.

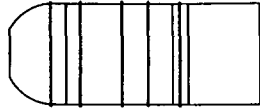


- Top row
- Side row
- ◇ Bottom row
- △ Base pressure

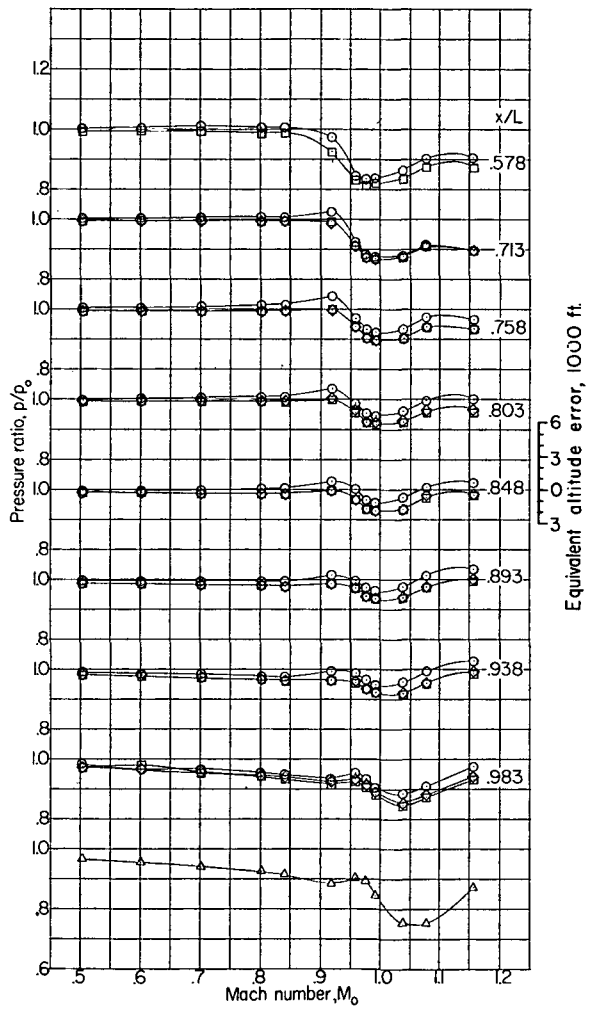
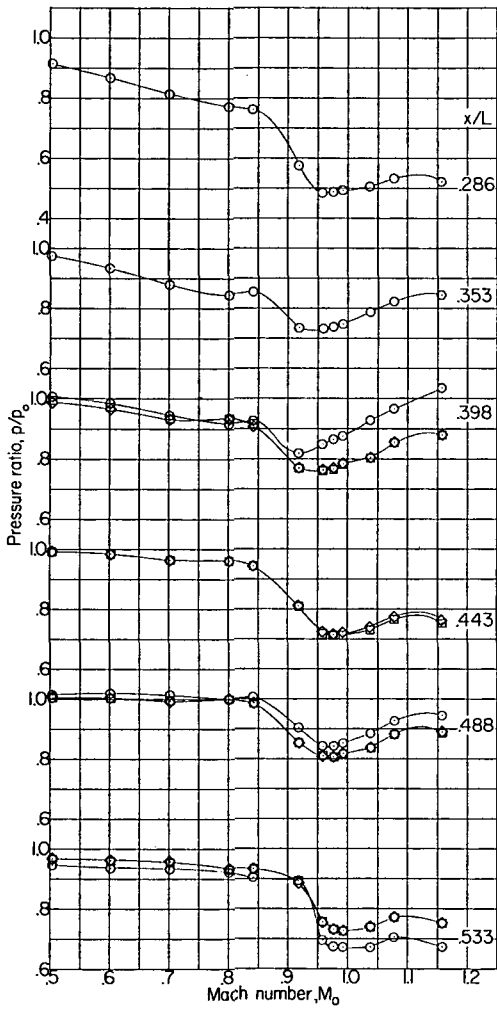


(b)  $\alpha = 2^\circ$ .

Figure 4.- Continued.



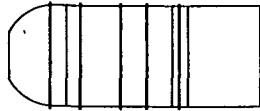
- Top row
- Side row
- ◇ Bottom row
- △ Base pressure



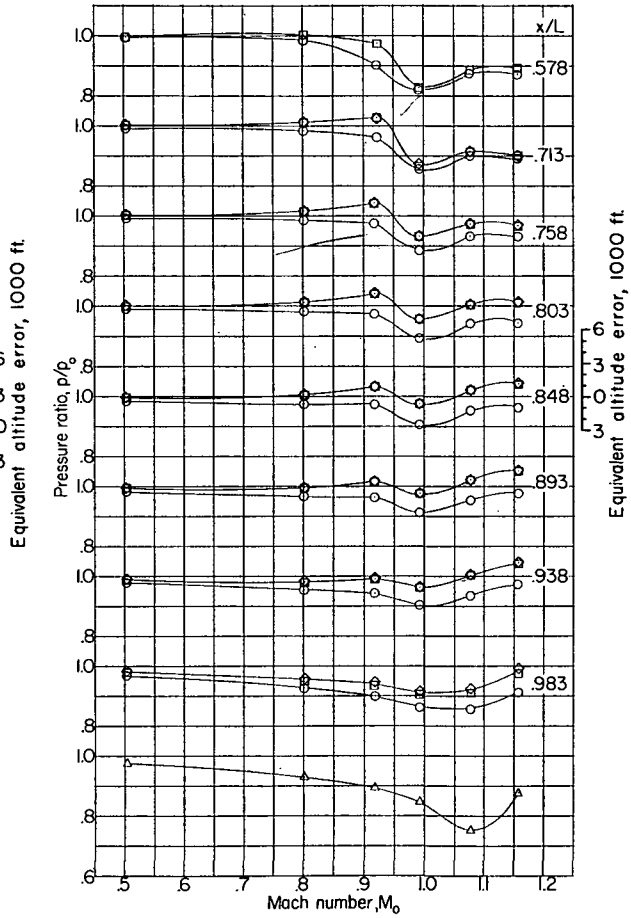
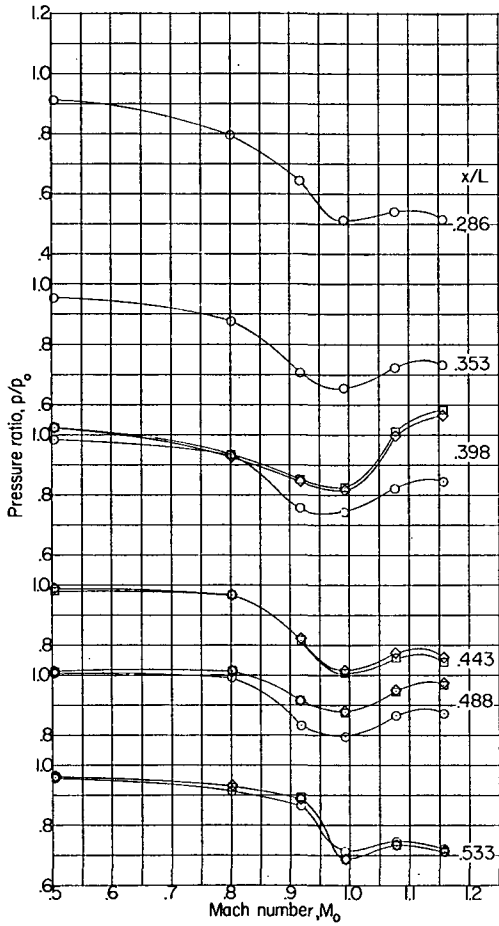
(c)  $\alpha = -2^\circ$ .

Figure 4.- Continued.





- Top row
- Side row
- ◇ Bottom row
- △ Base pressure

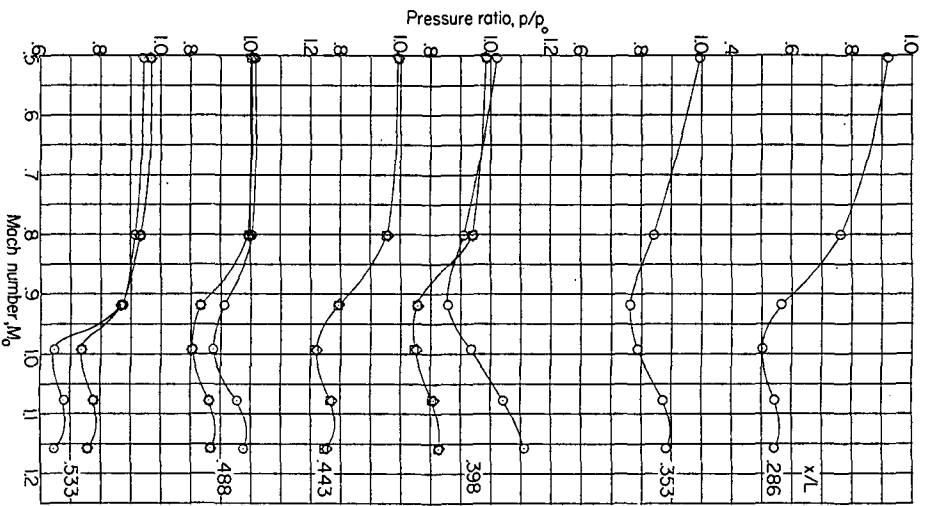


(d)  $\alpha = 4^\circ$ .

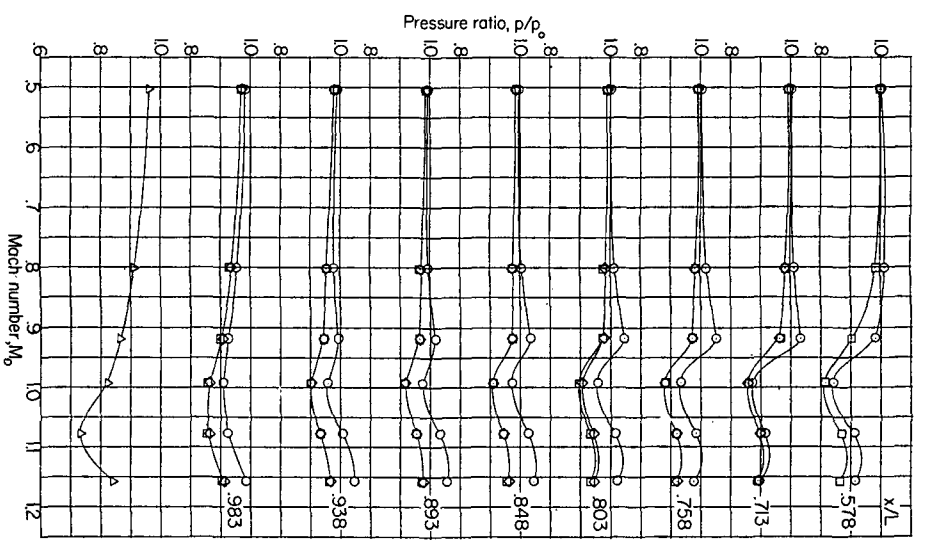
Figure 4.- Continued.



○ Top row  
 □ Side row  
 ◊ Bottom row  
 ▲ Base pressure



Equivalent altitude error, 1000 ft

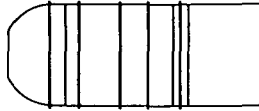


Equivalent altitude error, 1000 ft

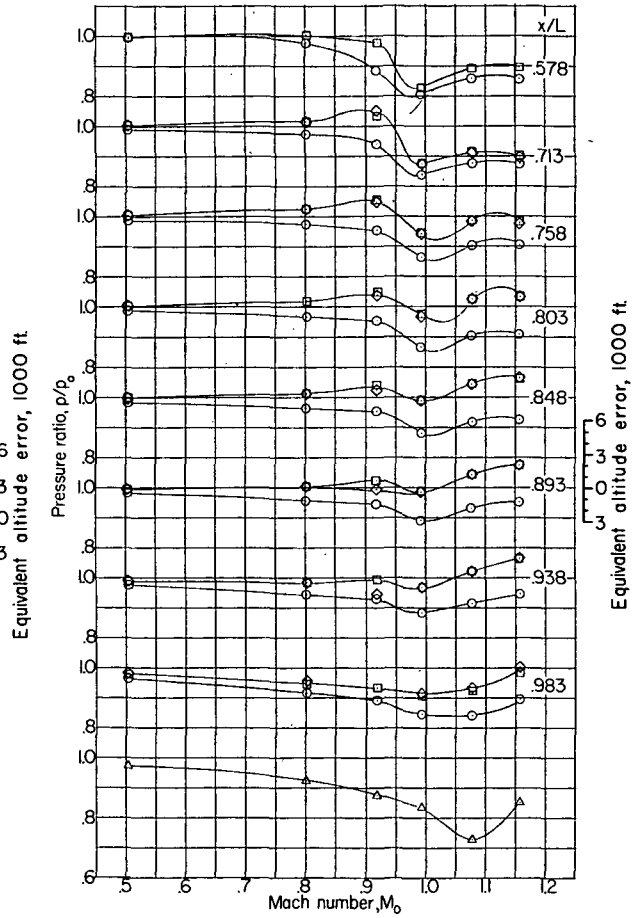
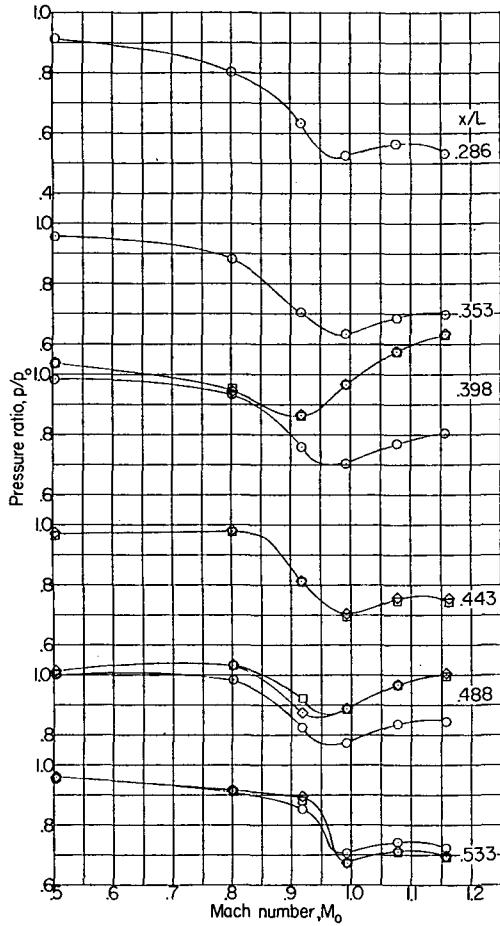
(e)  $\alpha = -4^\circ$

Figure 4.- Continued.



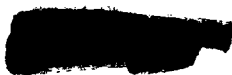


- Top row
- Side row
- ◇ Bottom row
- △ Base pressure



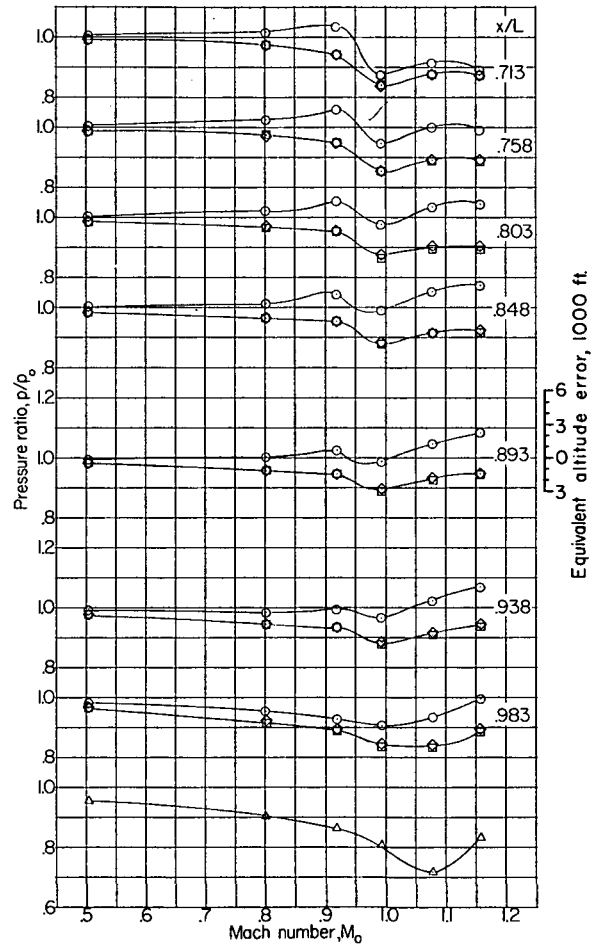
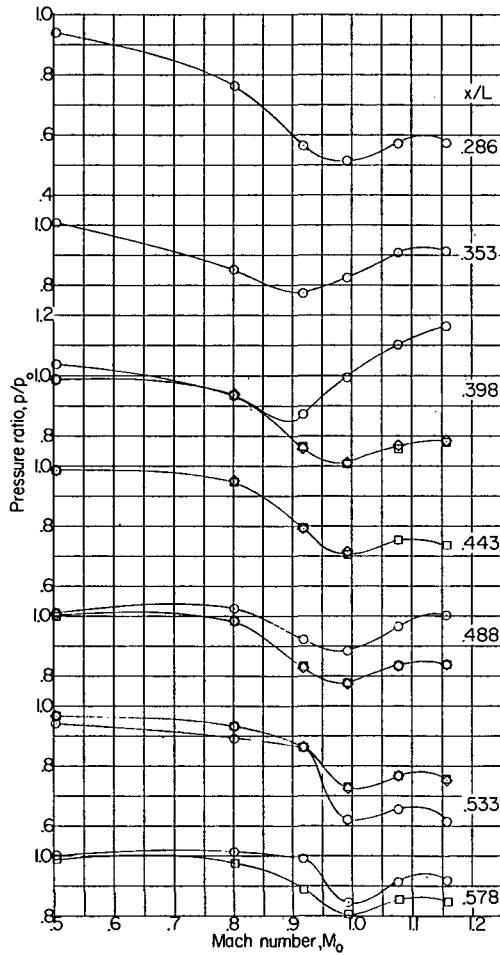
(f)  $\alpha = 6^\circ$ .

Figure 4.- Continued.





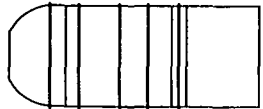
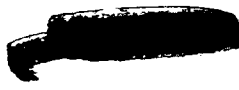
- Top row
- Side row
- ◇ Bottom row
- △ Base pressure



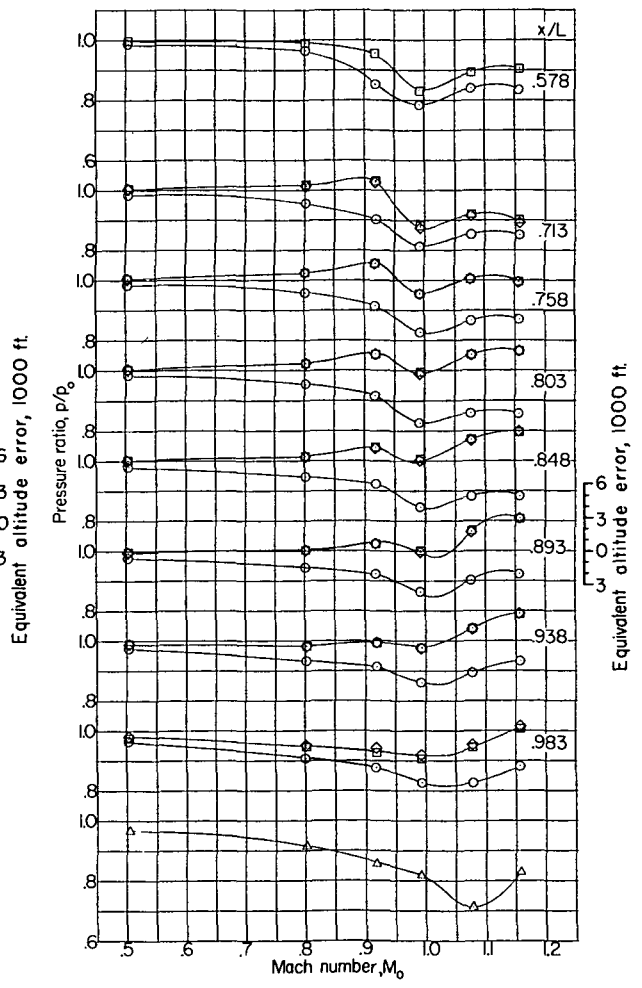
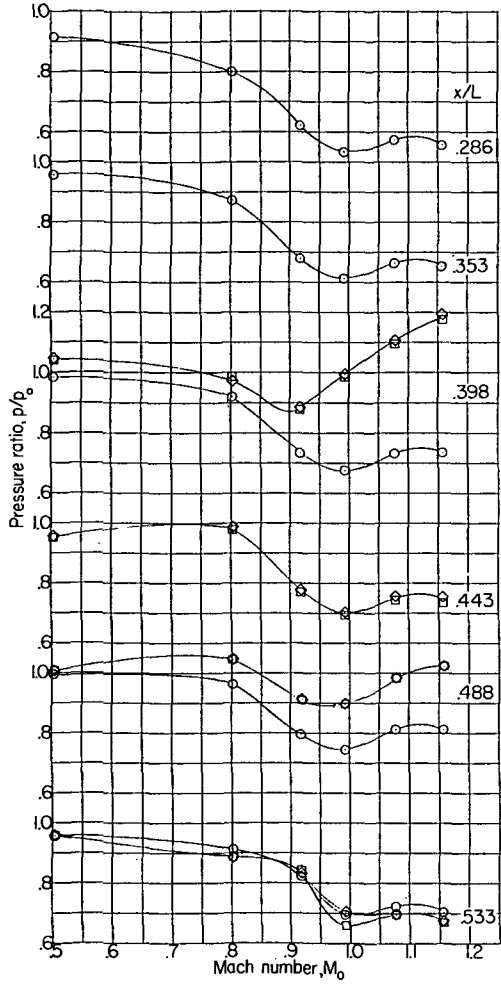
(g)  $\alpha = -6^\circ$ .

Figure 4.- Continued.





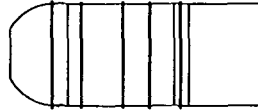
- Top row
- Side row
- ◇ Bottom row
- △ Base pressure



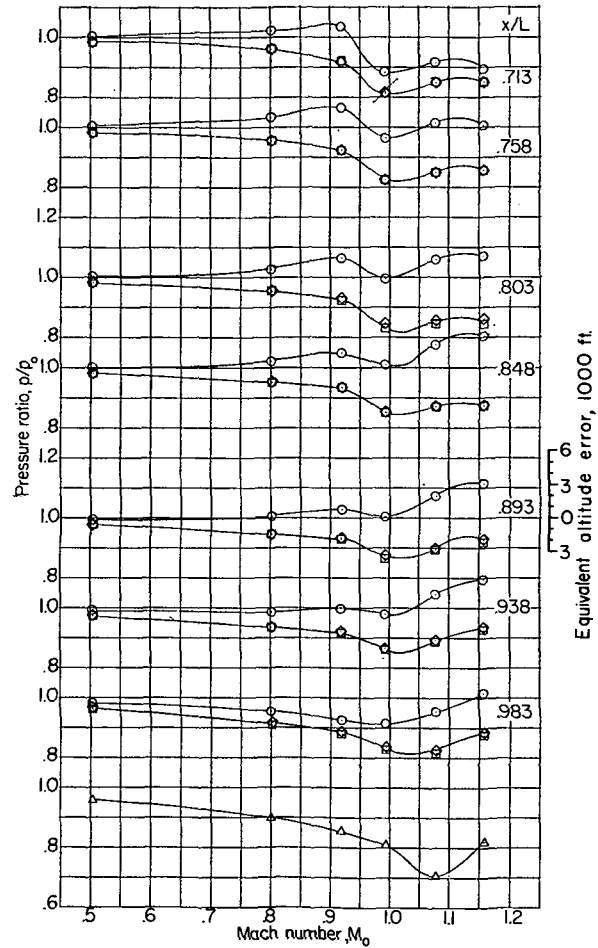
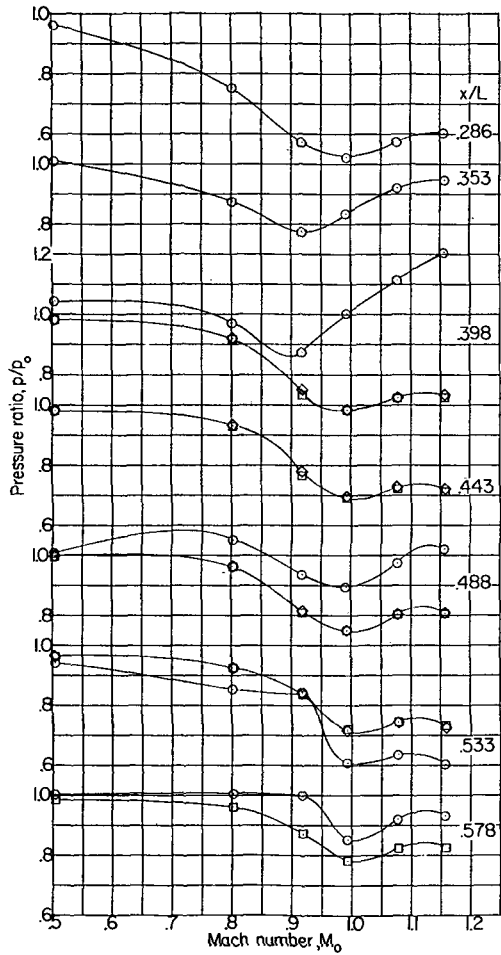
(h)  $\alpha = 8^\circ$ .

Figure 4.- Continued.





- Top row
- Side row
- ◇ Bottom row
- △ Base pressure

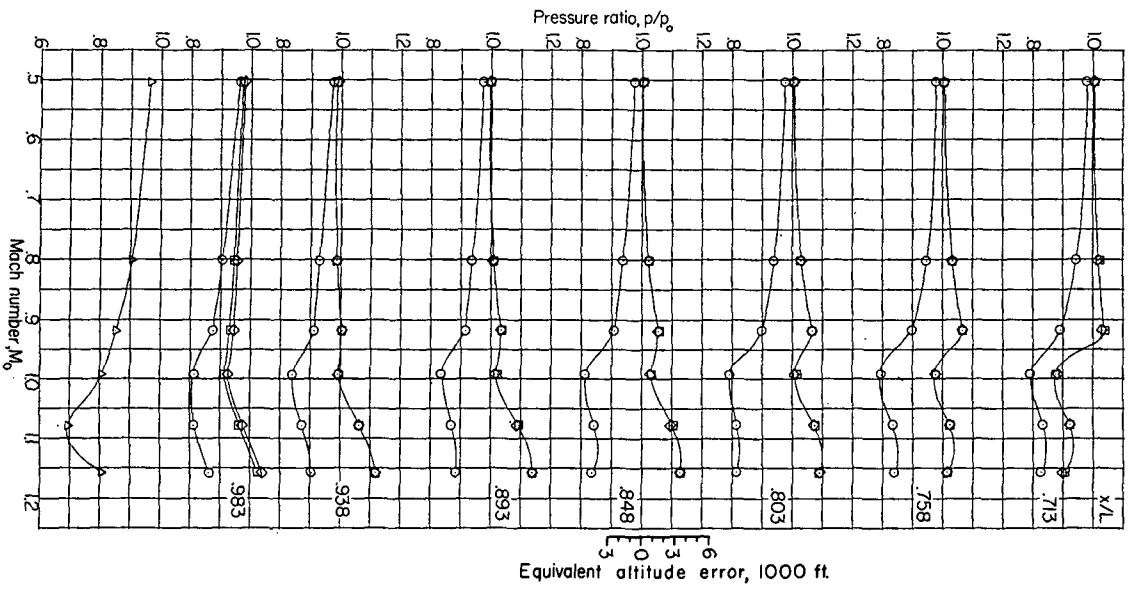
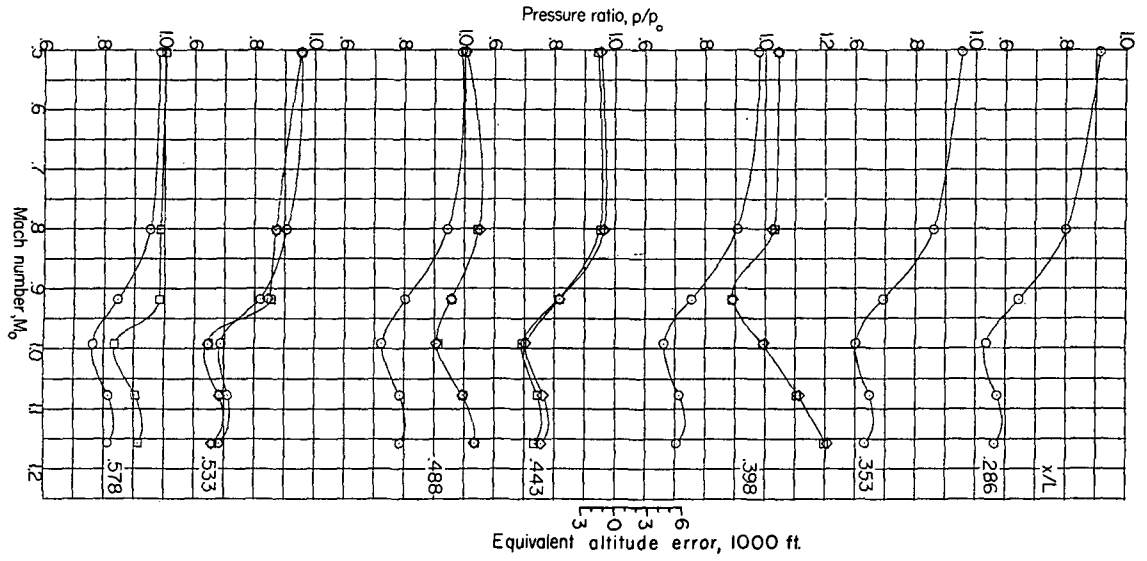


(i)  $\alpha = -8^\circ$ .

Figure 4.- Continued.



- Top row
- Side row
- ◇ Bottom row
- △ Base pressure

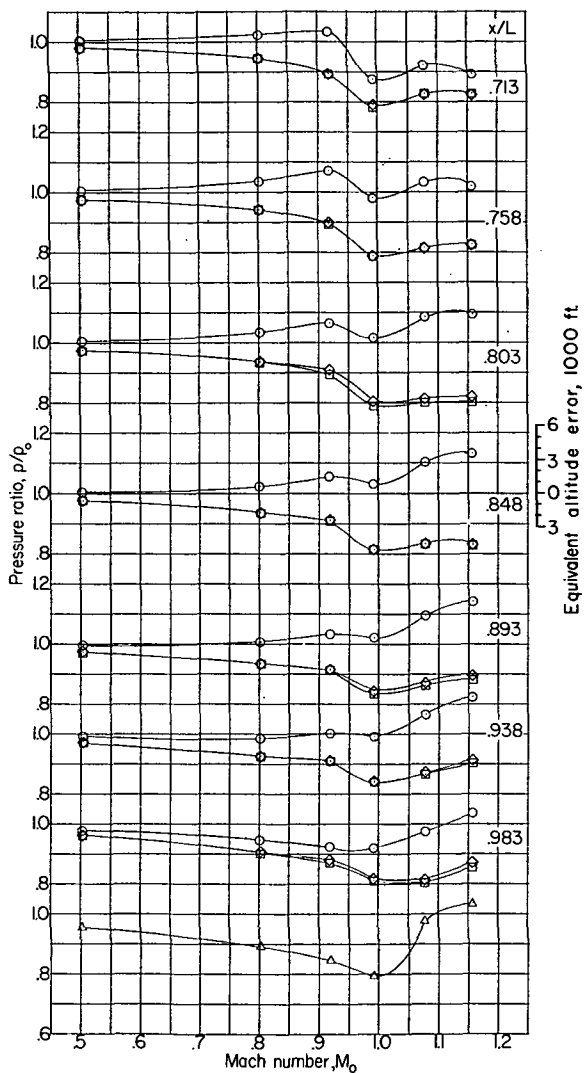
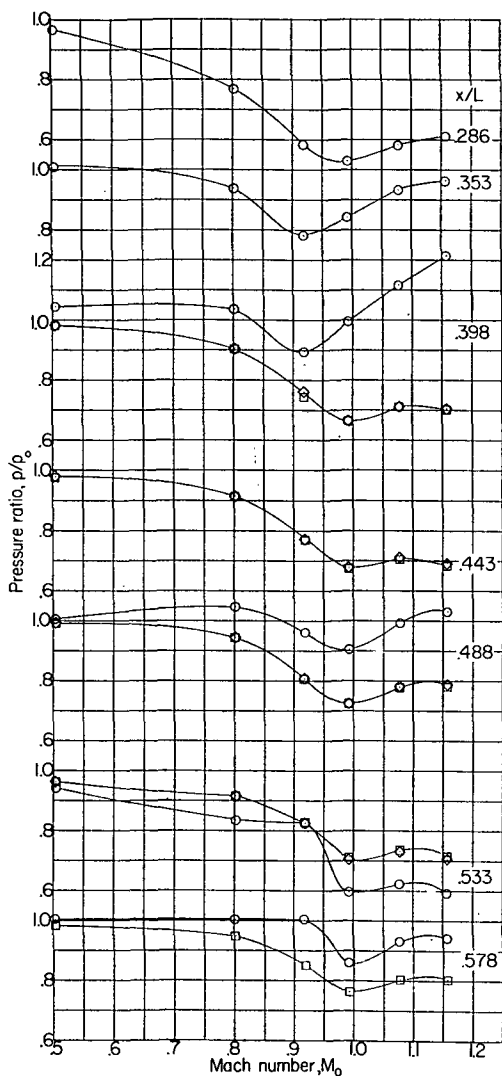


(j)  $\alpha = 10^\circ$ .

Figure 4.- Continued.



- Top row
- Side row
- ◇ Bottom row
- △ Base pressure



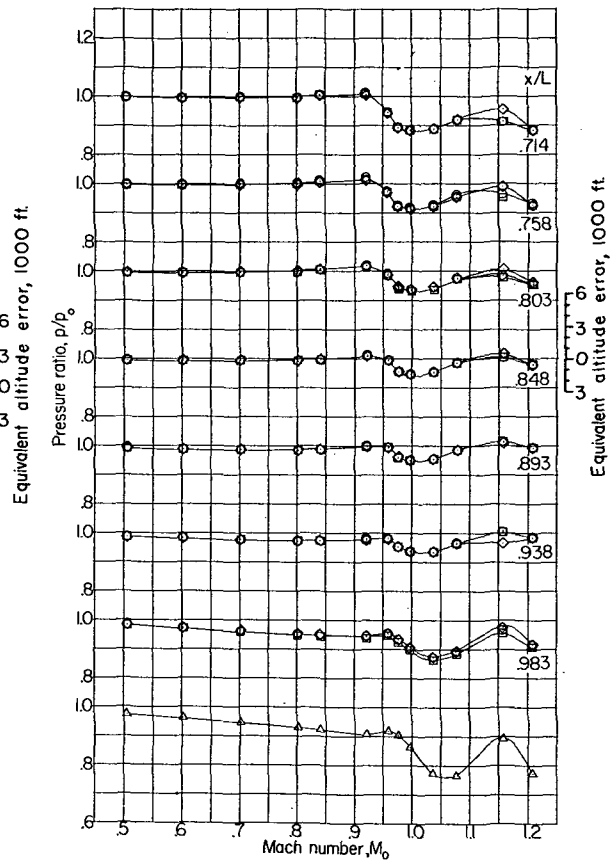
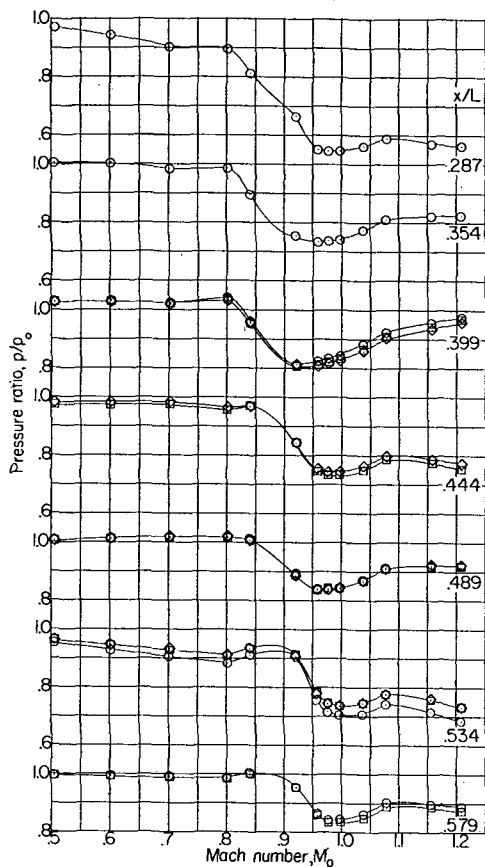
(k)  $\alpha = -10^\circ$ .

Figure 4.- Concluded.





- Top row
- Side row
- ◇ Bottom row
- △ Base pressure



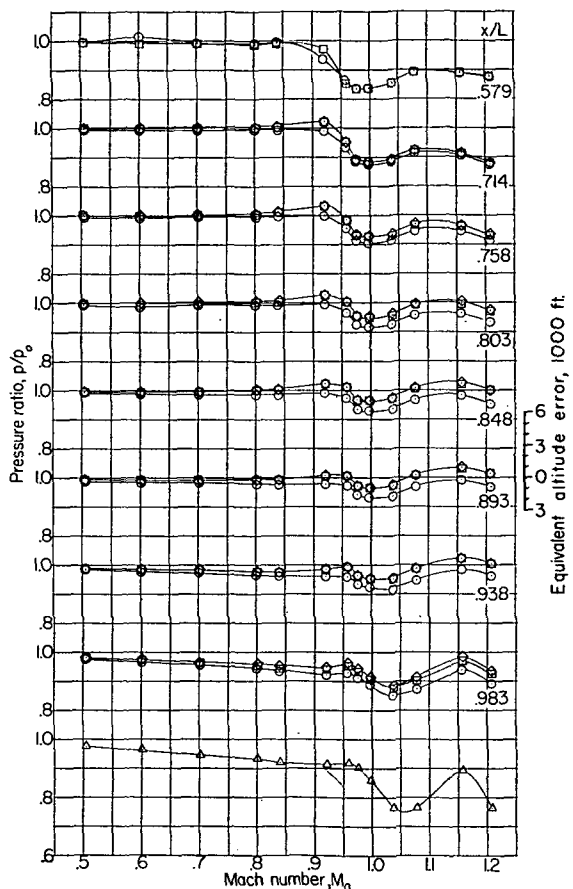
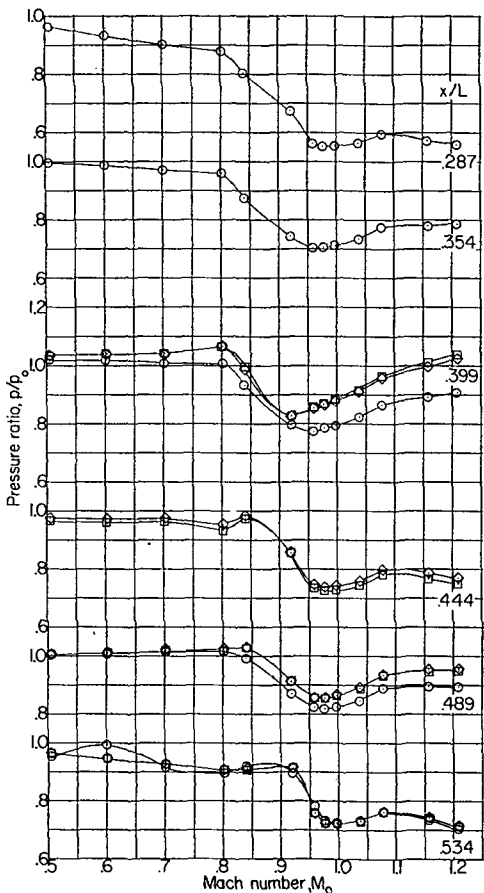
(a)  $\alpha = 0^\circ$ .

Figure 5.- The effect of Mach number and angle of attack on the local static-pressure ratio over the TX-21, nose B, configuration afterbody.





- Top row
- Side row
- ◇ Bottom row
- △ Base pressure

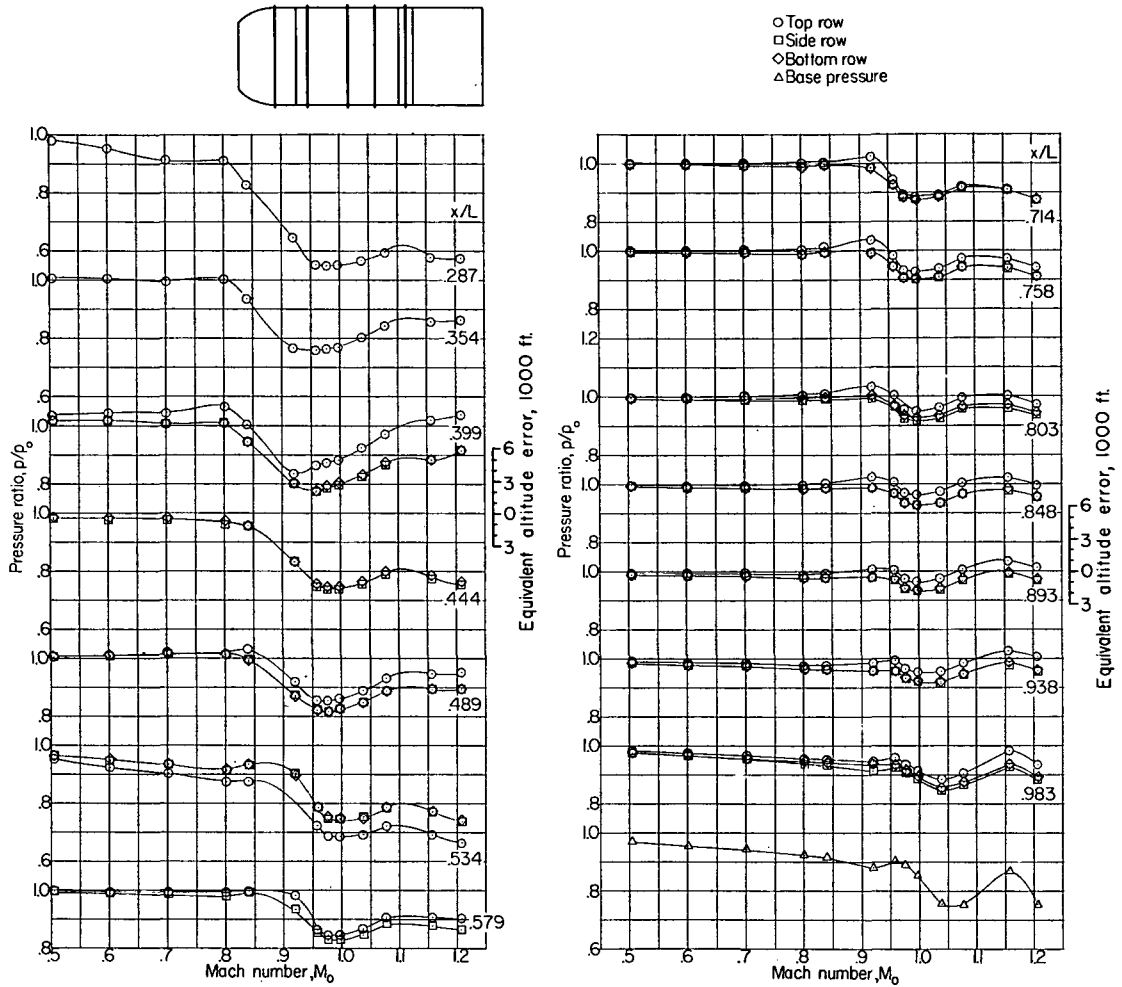


(b)  $\alpha = 2^\circ$ .

Figure 5.- Continued.

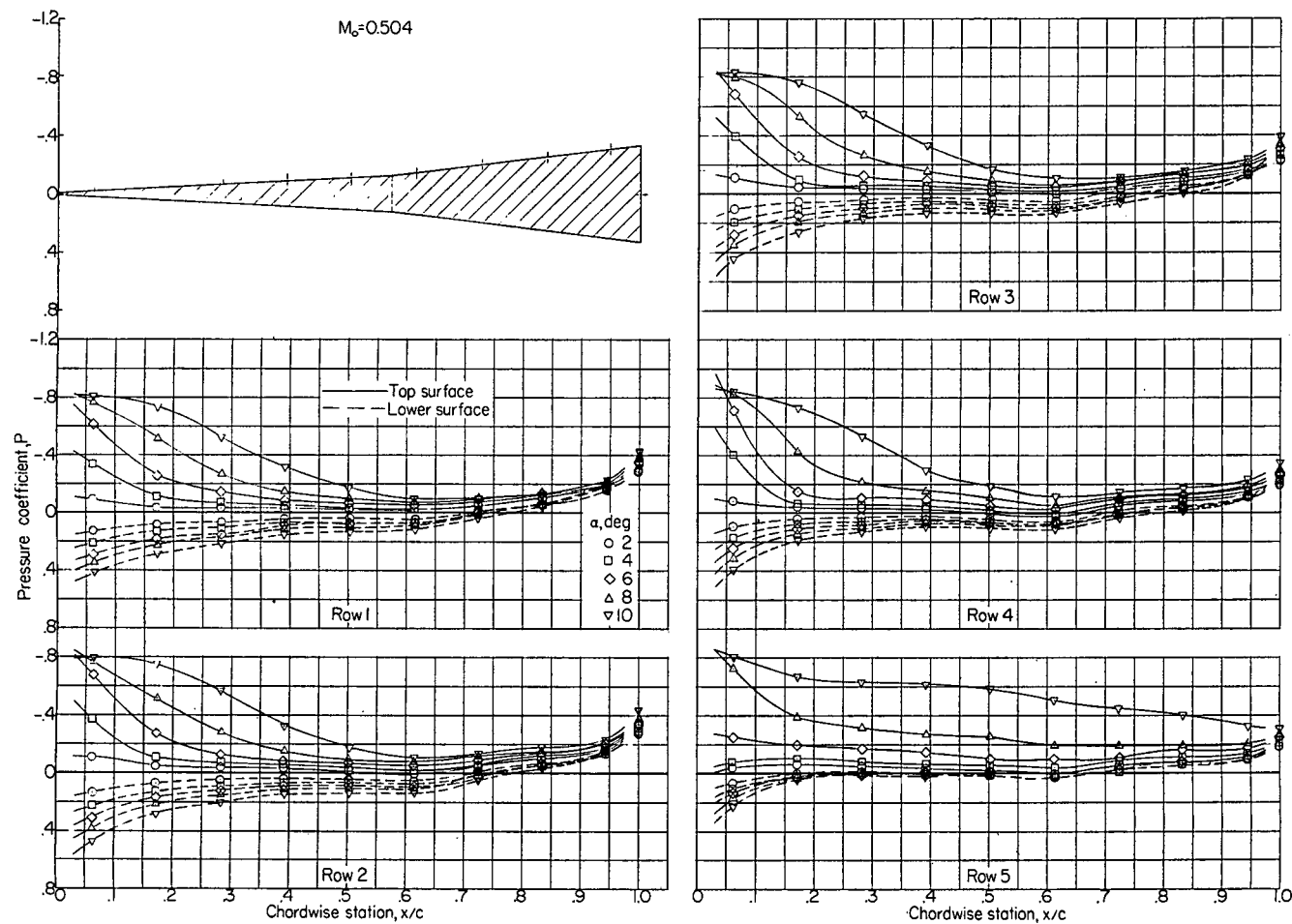






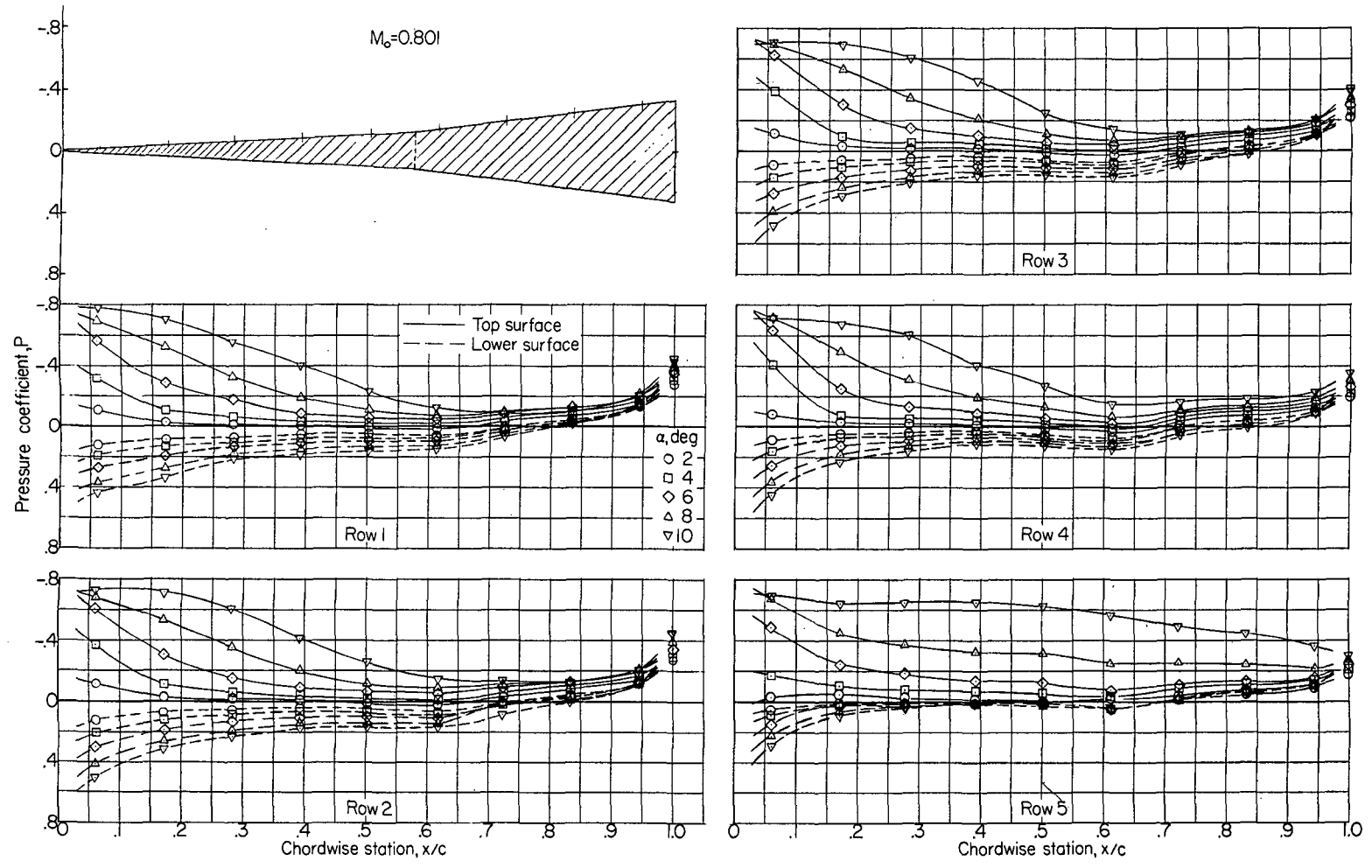
(c)  $\alpha = -2^\circ$ .

Figure 5.- Concluded.



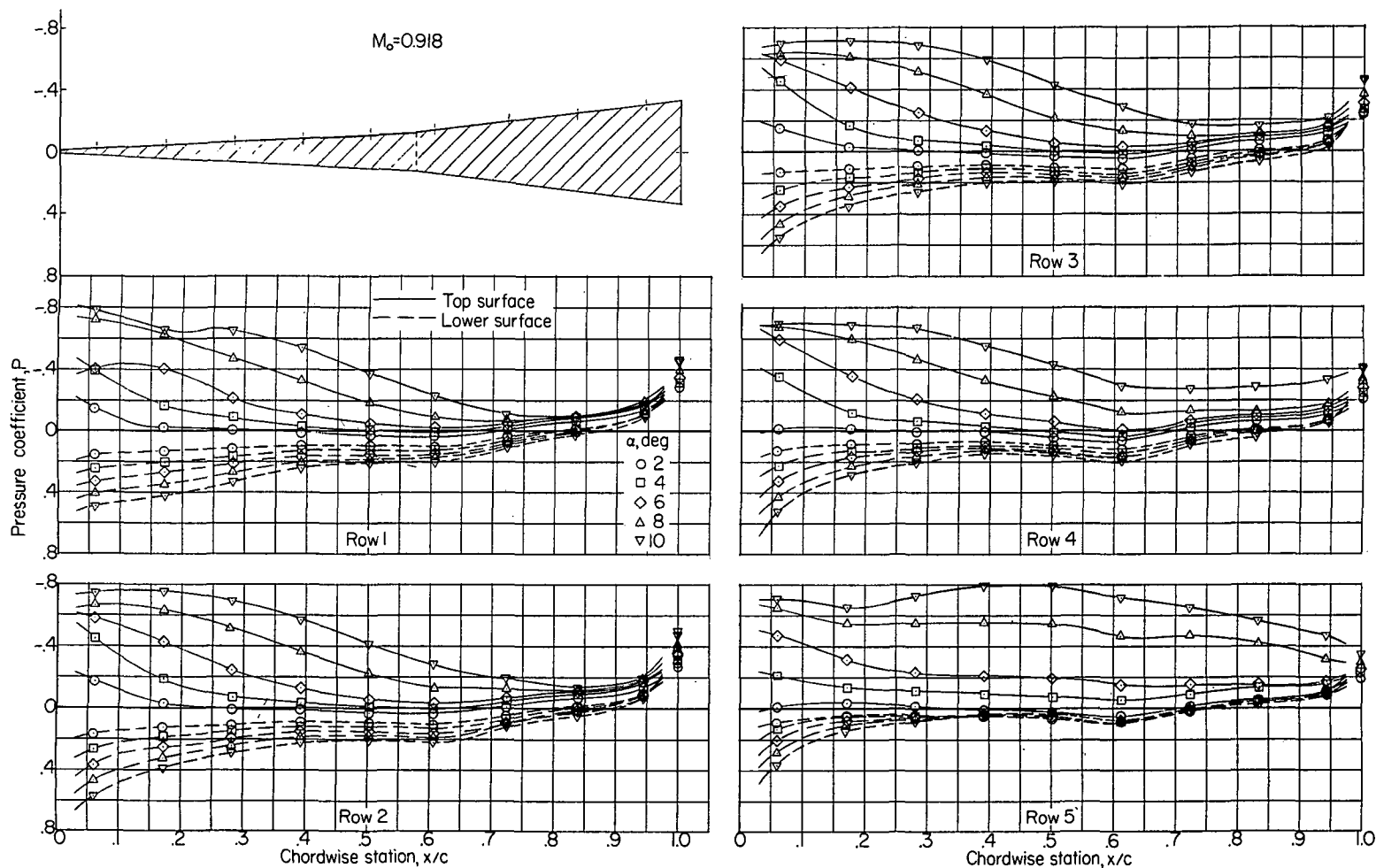
(a)  $M_0 = 0.504$ .

Figure 6.- Pressure distributions over the fin surfaces at various Mach numbers and angles of attack for the TX-21, nose A, configuration.



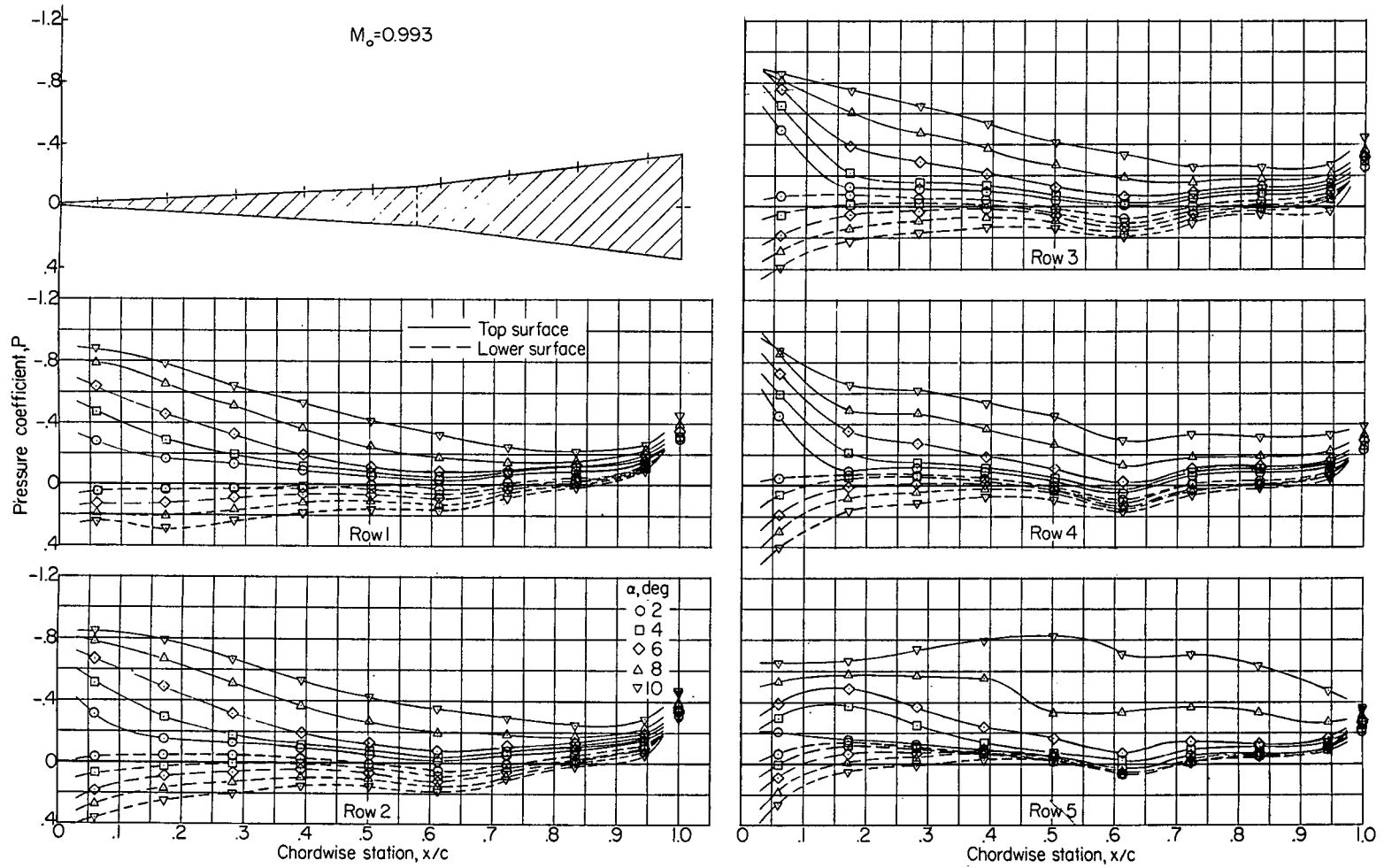
(b)  $M_0 = 0.801$ .

Figure 6.- Continued.



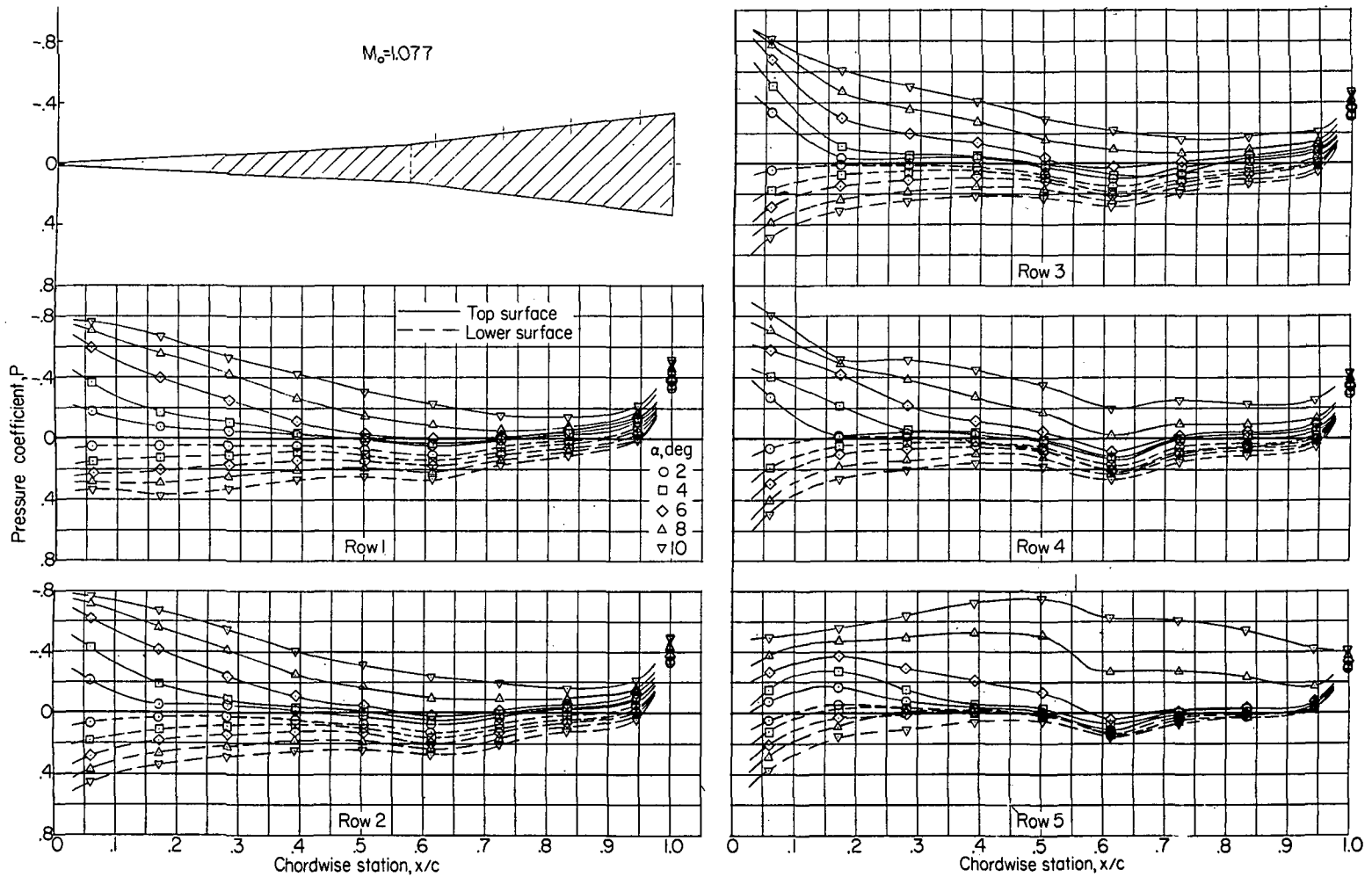
(c)  $M_0 = 0.918$ .

Figure 6.- Continued.



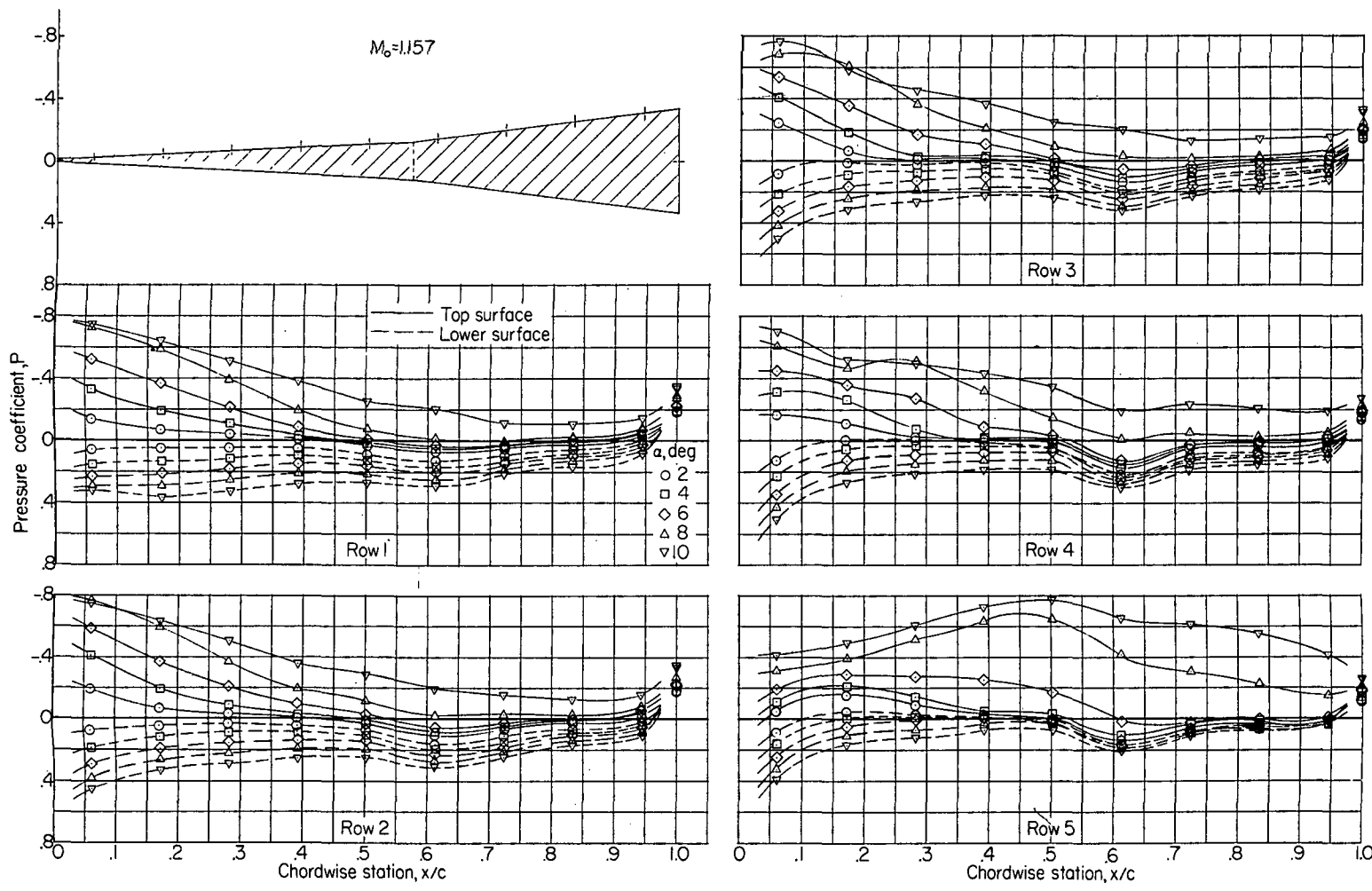
(d)  $M_0 = 0.993$ .

Figure 6.- Continued.



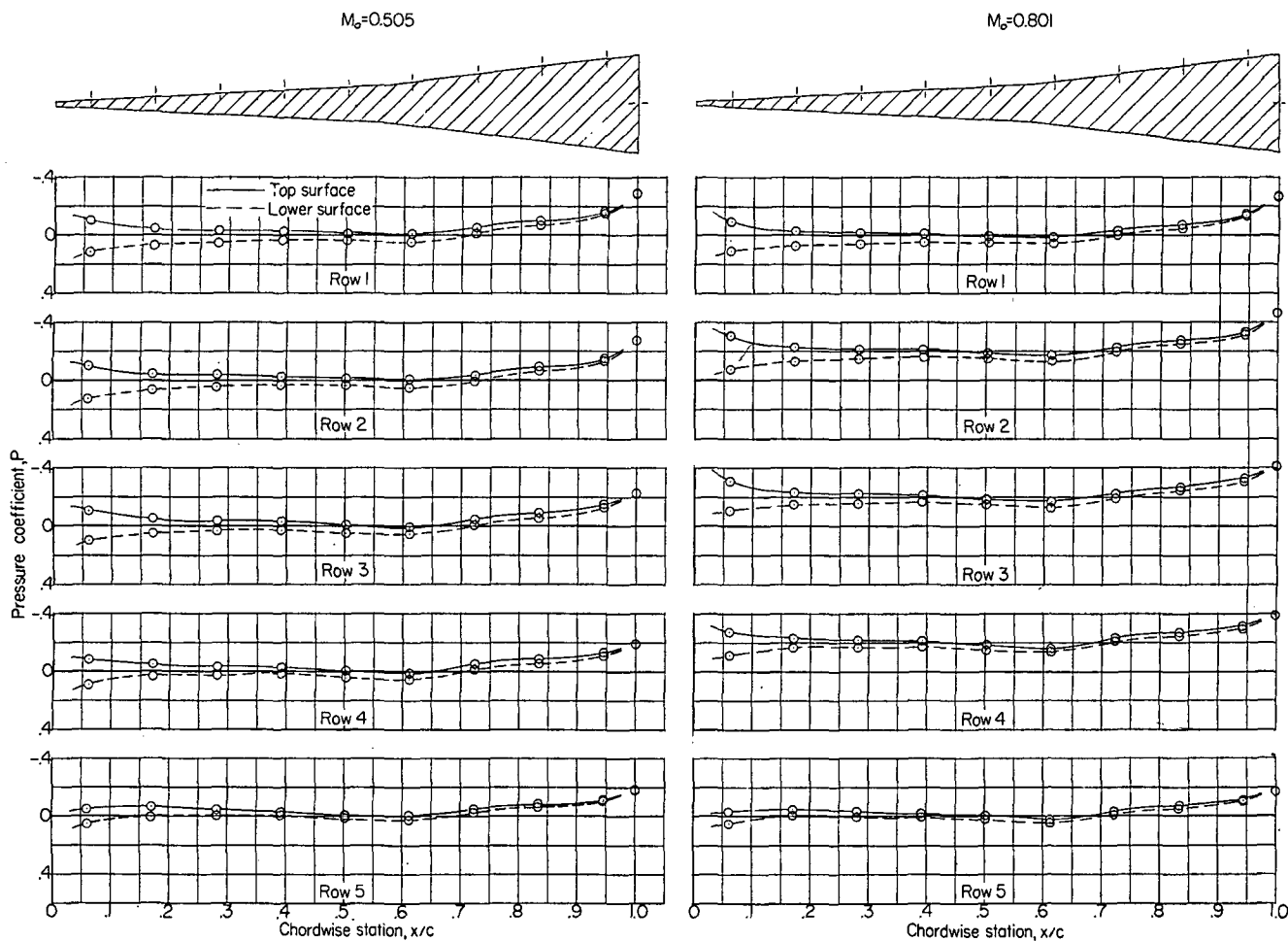
(e)  $M_0 = 10.77$ .

Figure 6.- Continued.



(f)  $M_0 = 1.157$ .

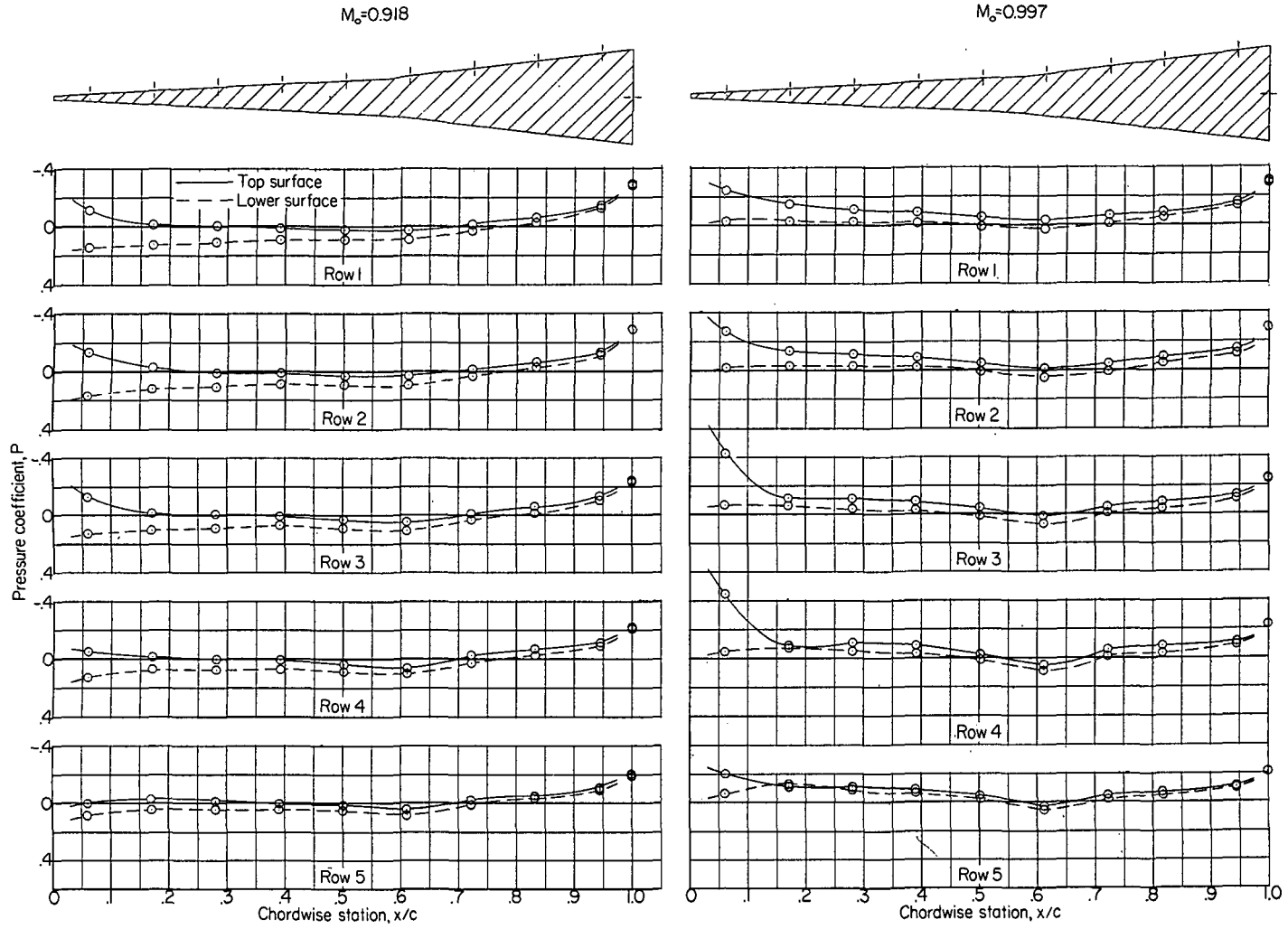
Figure 6.- Concluded.



(a)  $M_0 = 0.505$  and  $0.801$ .

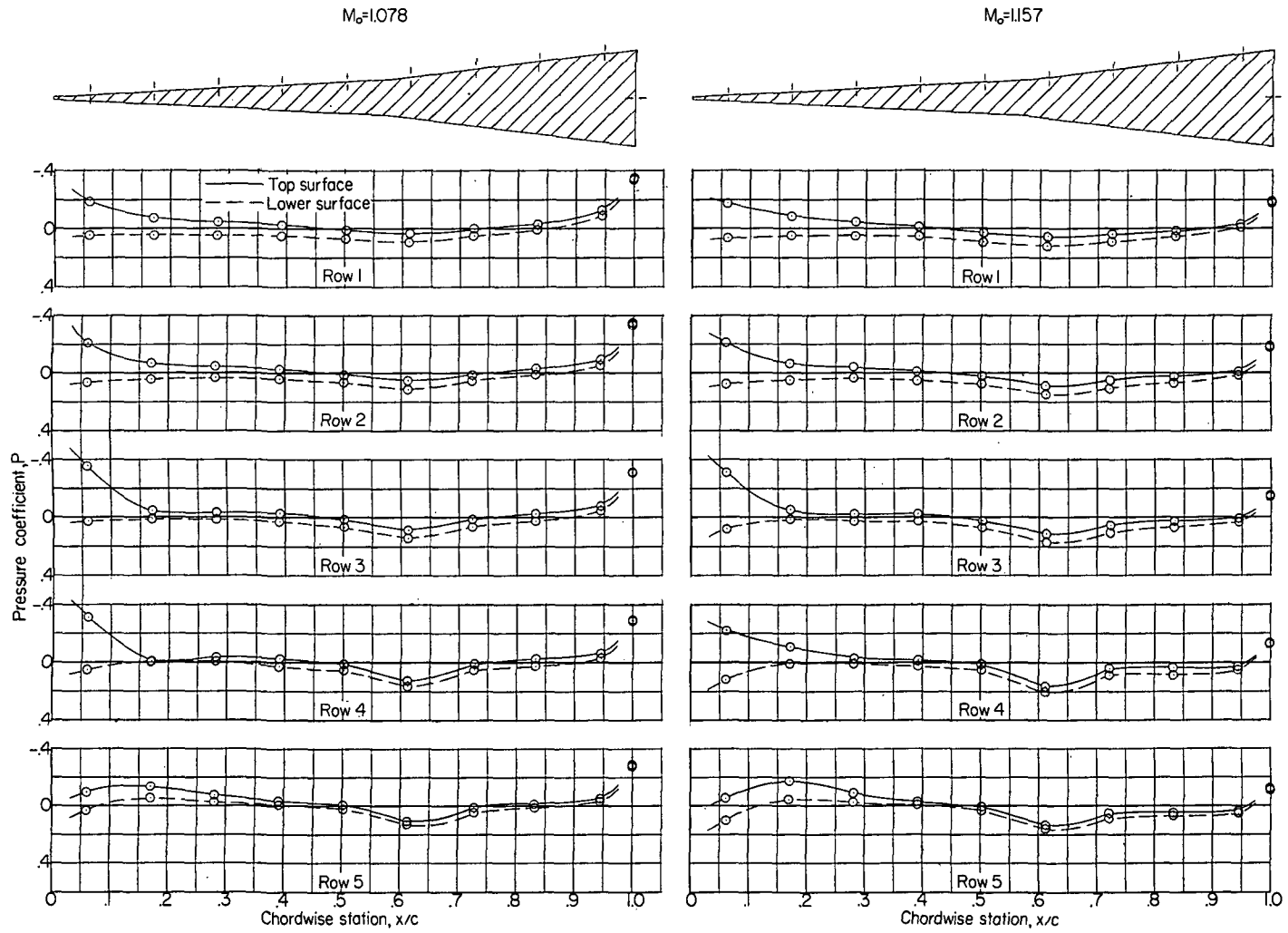
Figure 7.- Pressure distributions over the fin surfaces at various Mach numbers and angles of attack for the TX-21, nose B, configuration.





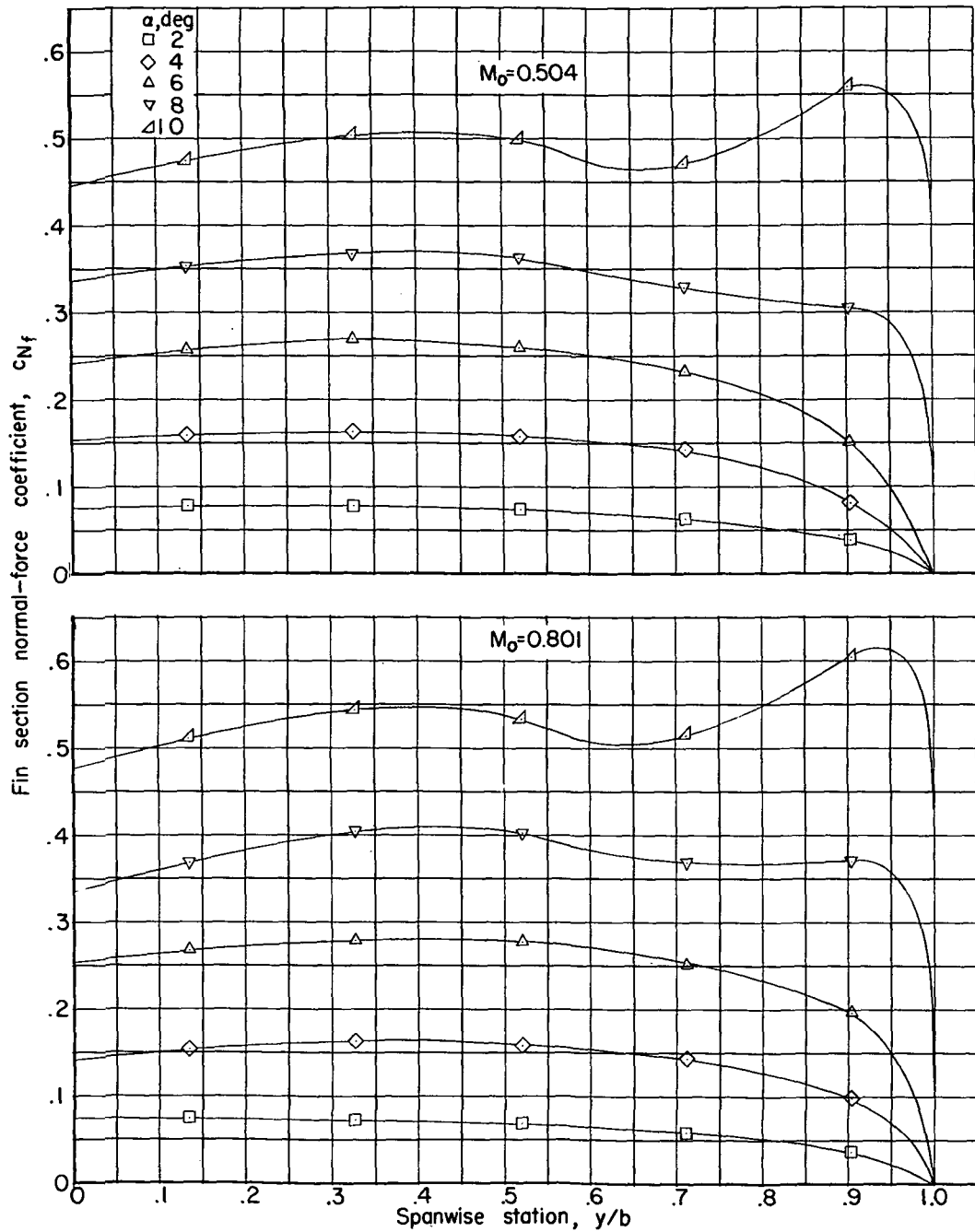
(b)  $M_0 = 0.918$  and  $0.997$ .

Figure 7.- Continued.



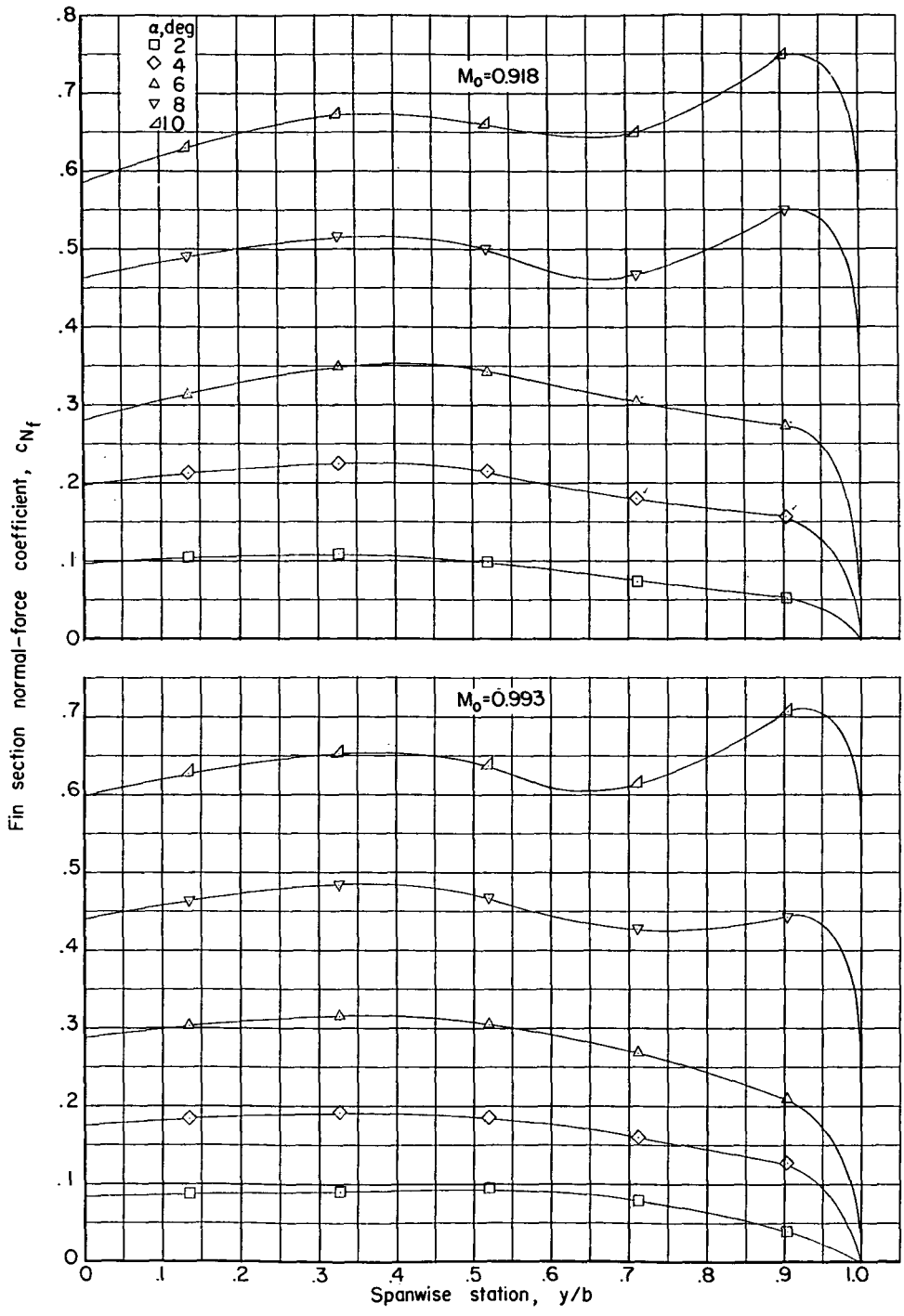
(c)  $M_0 = 1.078$  and  $1.157$ .

Figure 7.- Concluded.



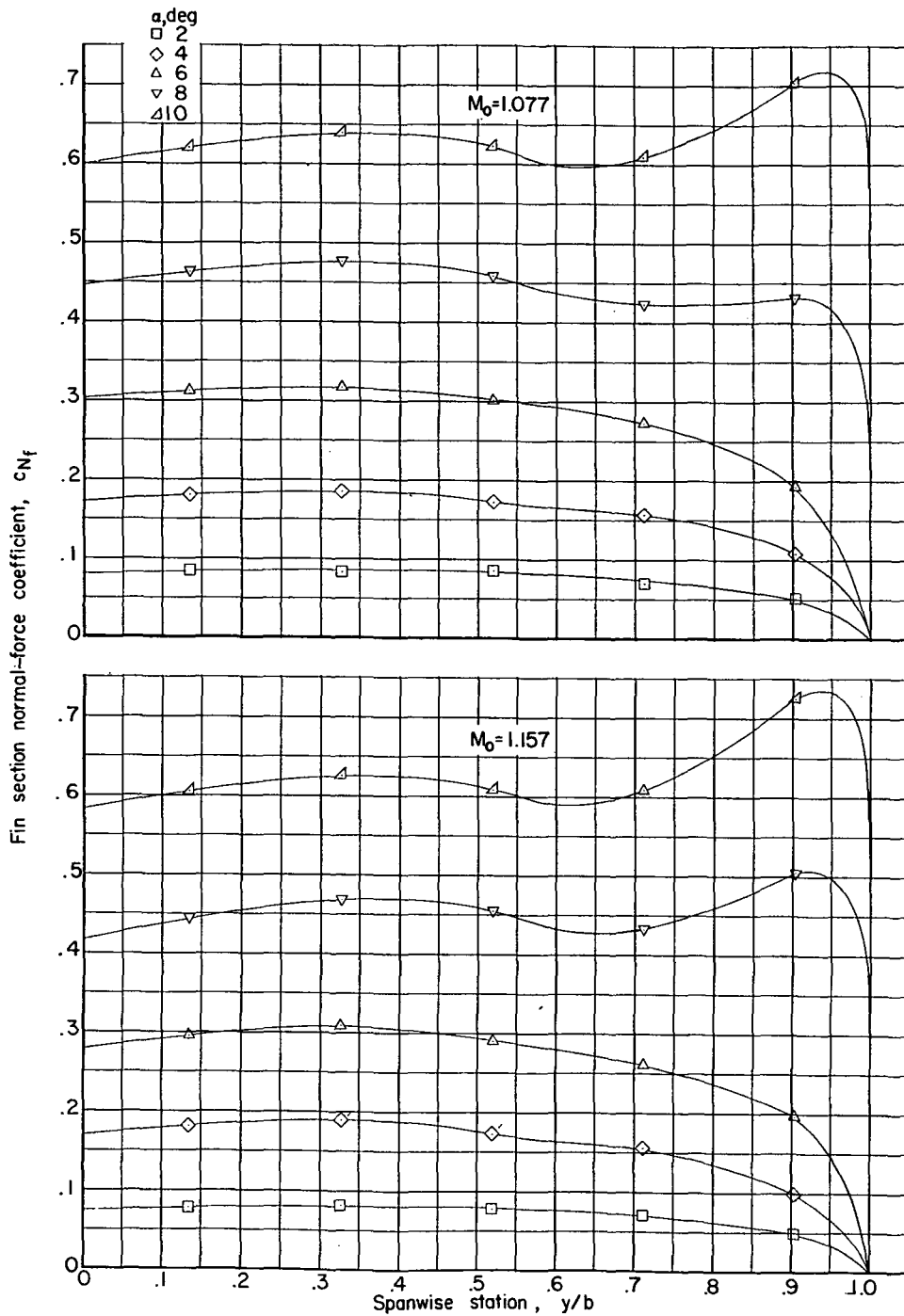
(a)  $M_0 = 0.504$  and  $0.801$ .

Figure 8.- The spanwise variation of fin section normal-force coefficient with Mach number and angle of attack for the TX-21, nose A, configuration.



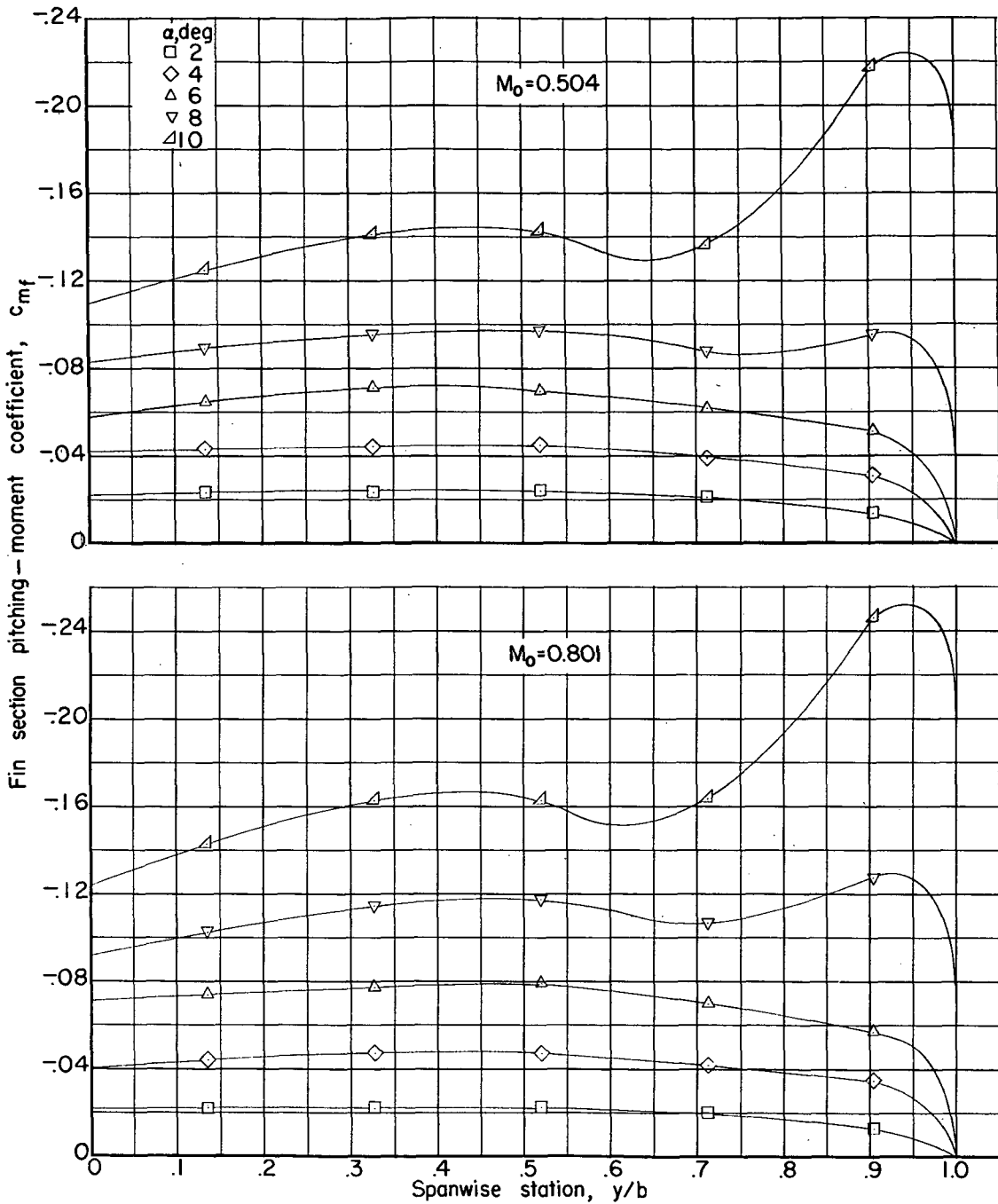
(b)  $M_0 = 0.918$  and  $0.993$ .

Figure 8.- Continued.



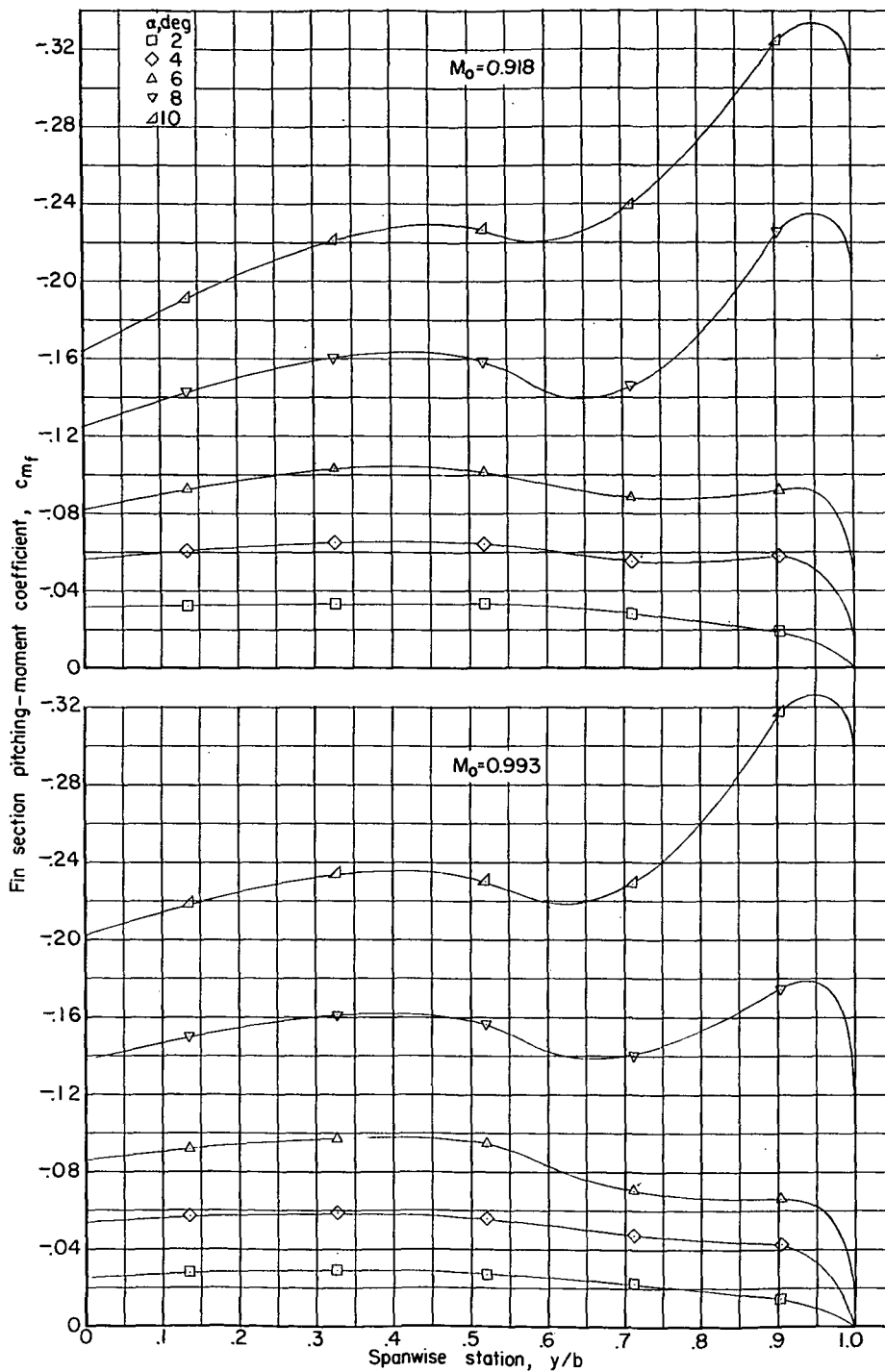
(c)  $M_0 = 1.077$  and  $1.157$ .

Figure 8.- Concluded.



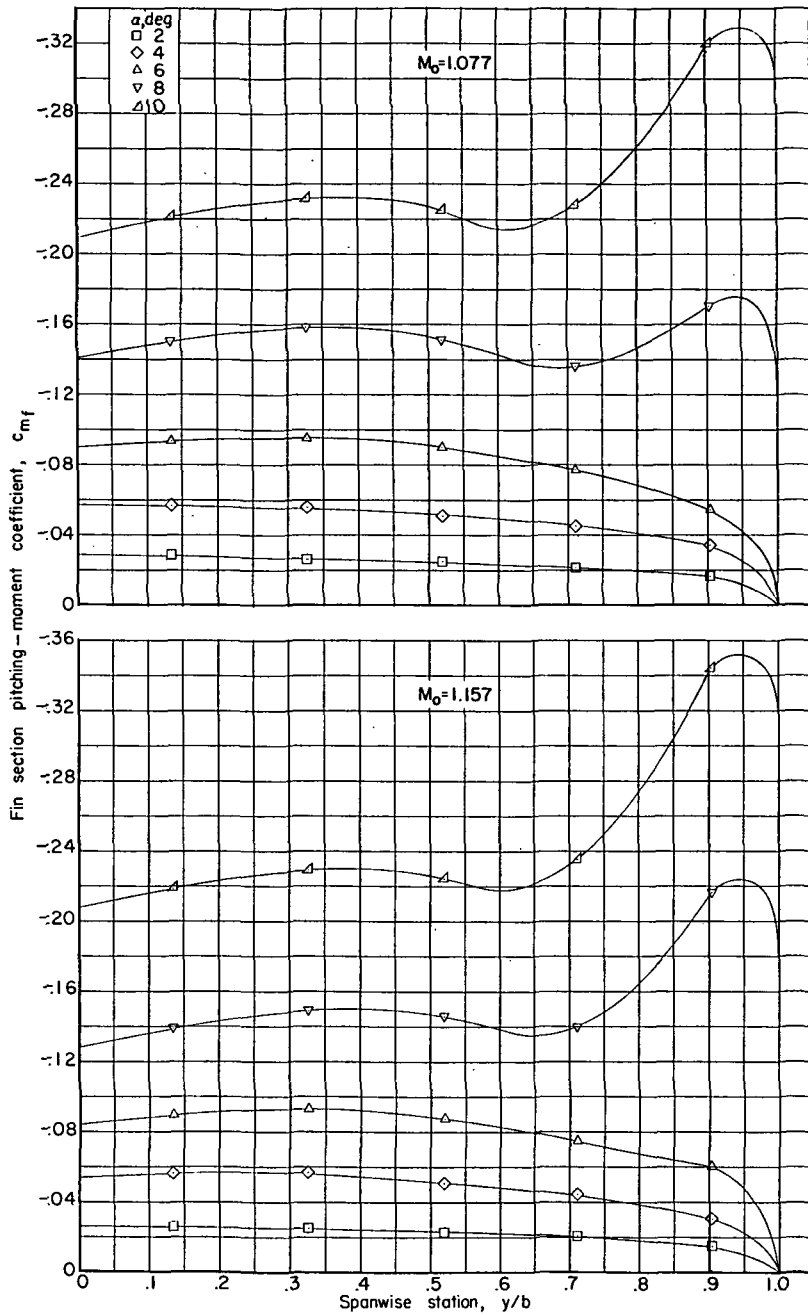
(a)  $M_0 = 0.504$  and  $0.801$ .

Figure 9.- The spanwise variation of fin section pitching-moment coefficient with Mach number and angle of attack for the TX-21, nose A, configuration.



(b)  $M_0 = 0.918$  and  $0.993$ .

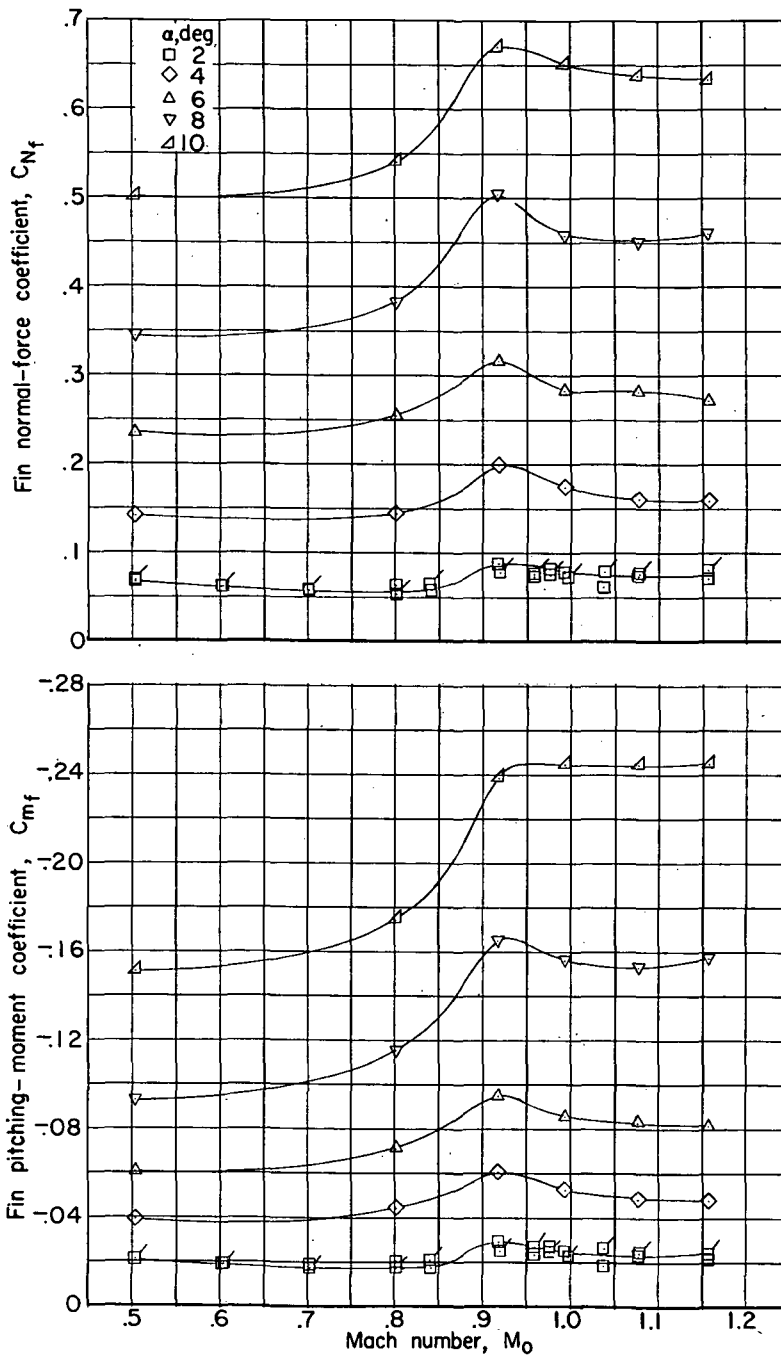
Figure 9.- Continued.



(c)  $M_0 = 1.077$  and  $1.157$ .

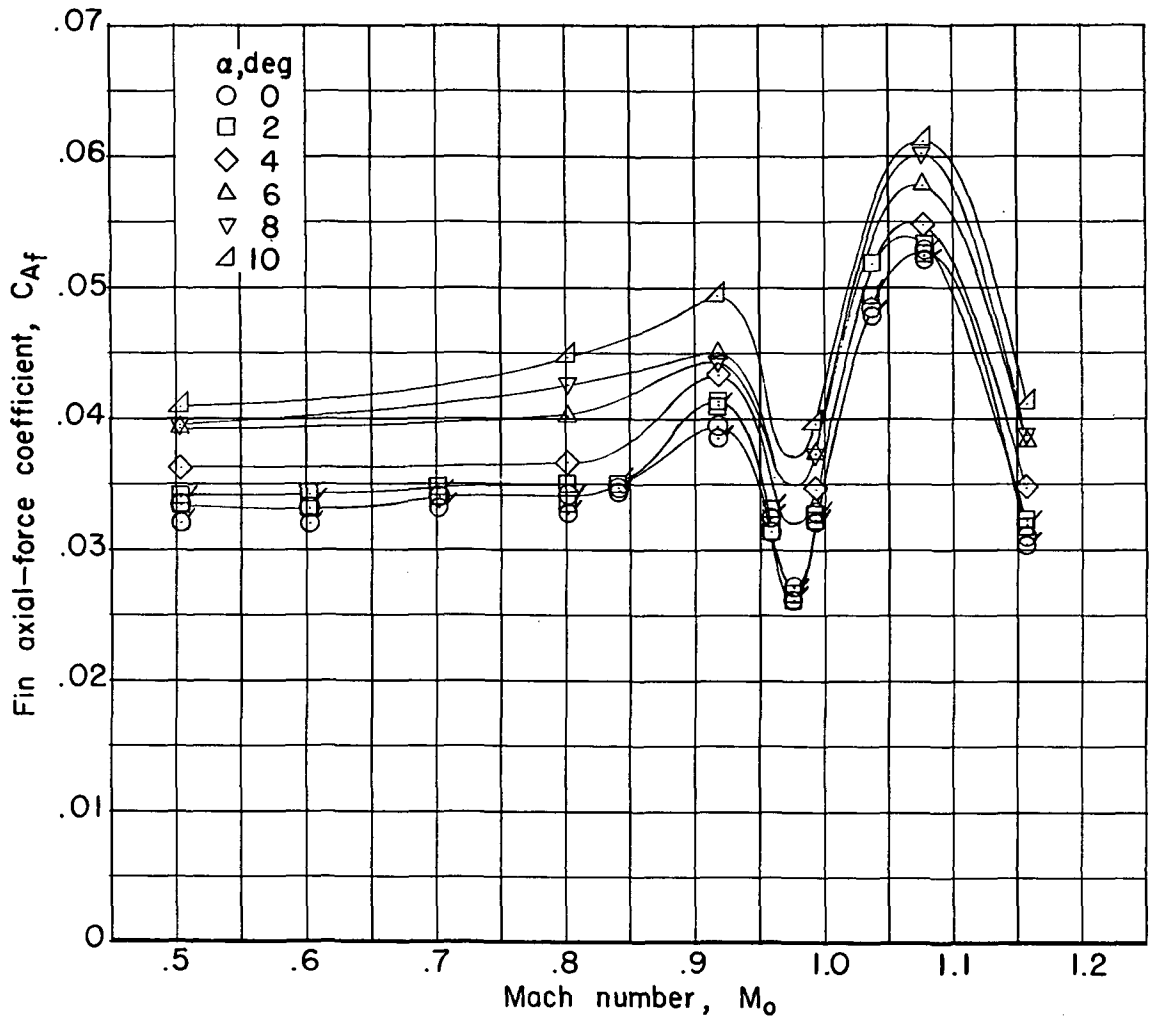
Figure 9.- Concluded.





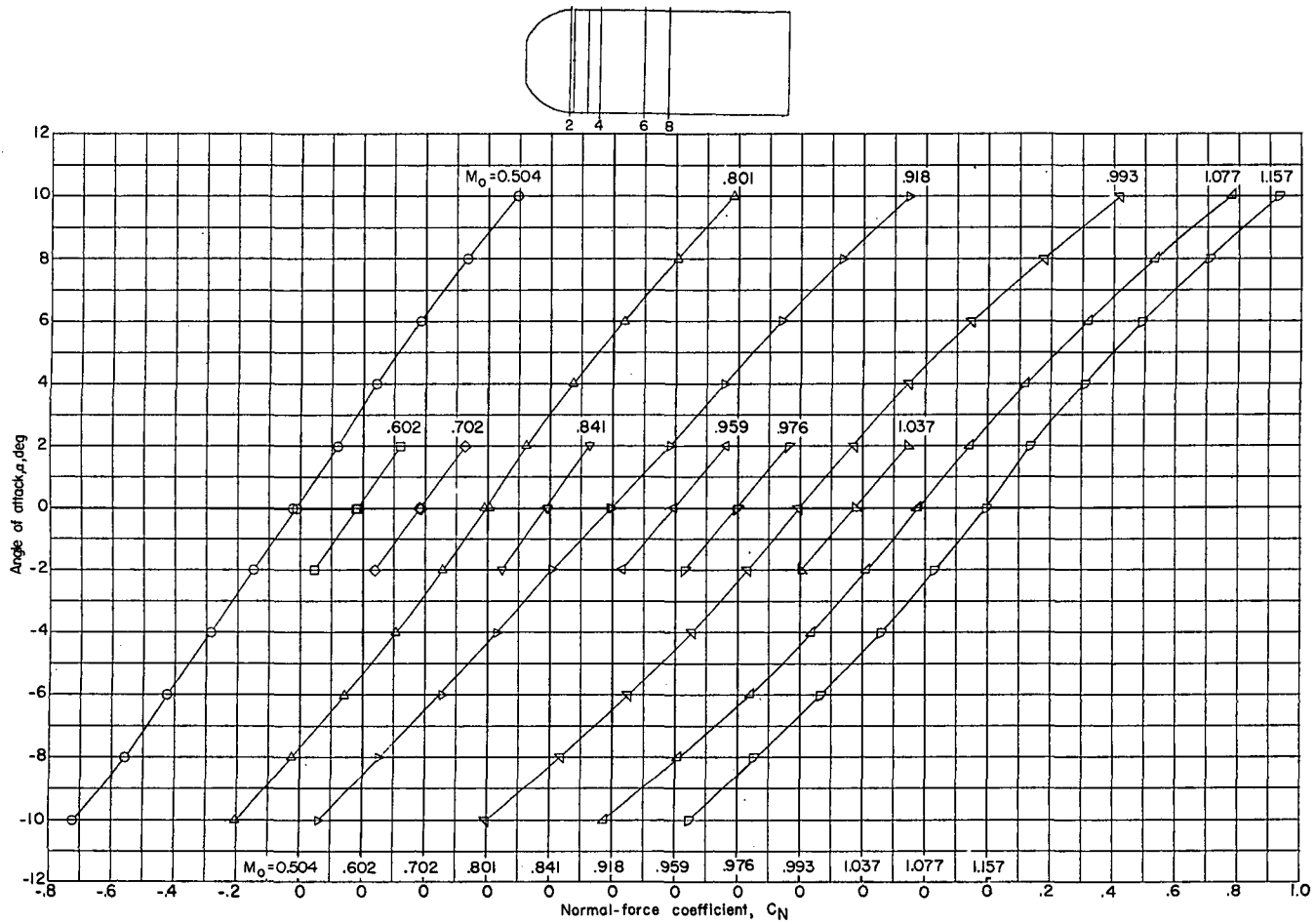
(a) Normal force and pitching moment.

Figure 10.-The variation of total fin forces with Mach number and angle of attack for the TX-21 configurations. Flagged symbols are for the nose B configuration.



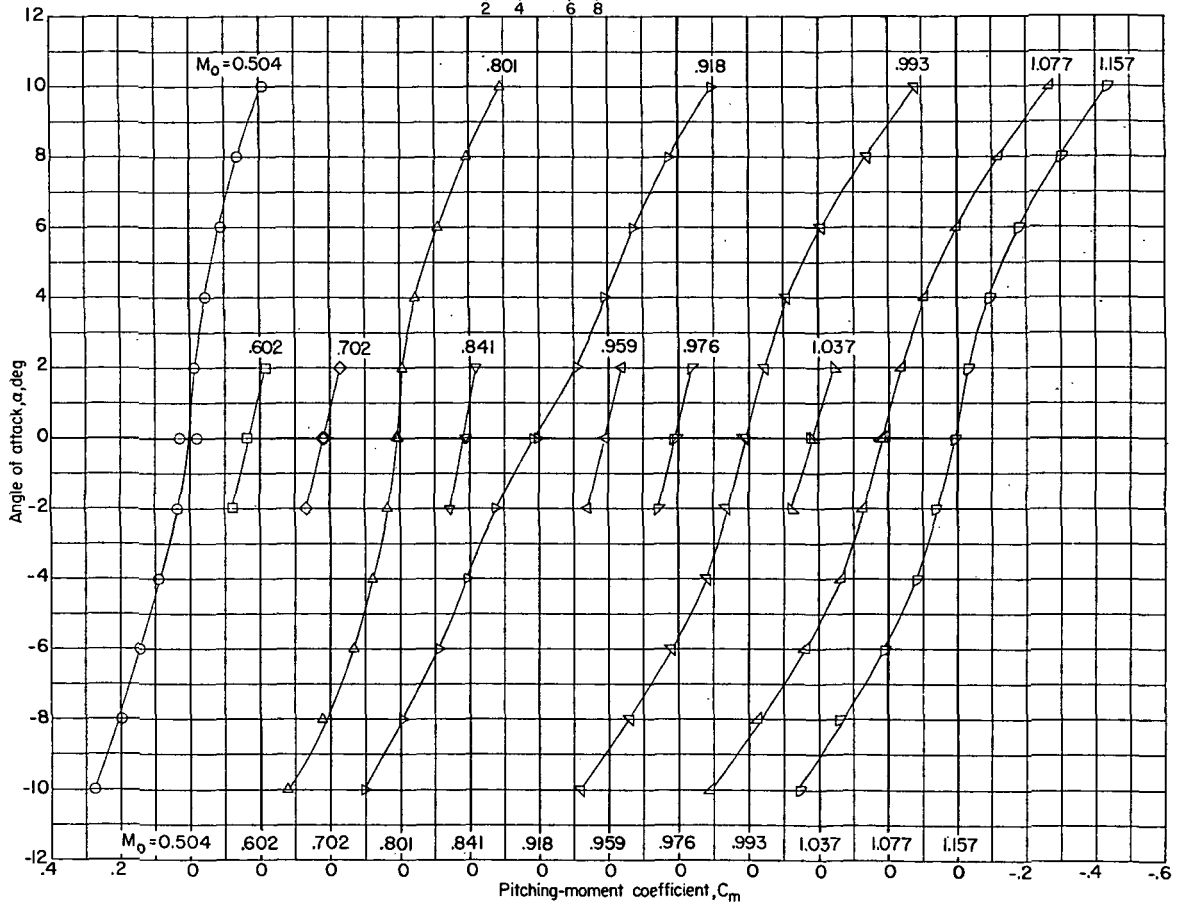
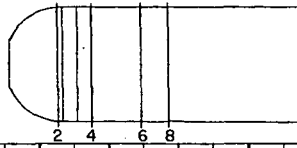
(b) Axial force.

Figure 10.- Concluded.



(a) Normal force.

Figure 11.- The variation of normal-force and pitching-moment coefficients with angle of attack at different Mach numbers for the TX-21, nose A, configuration.



(b) Pitching moment.

Figure 11.- Concluded.

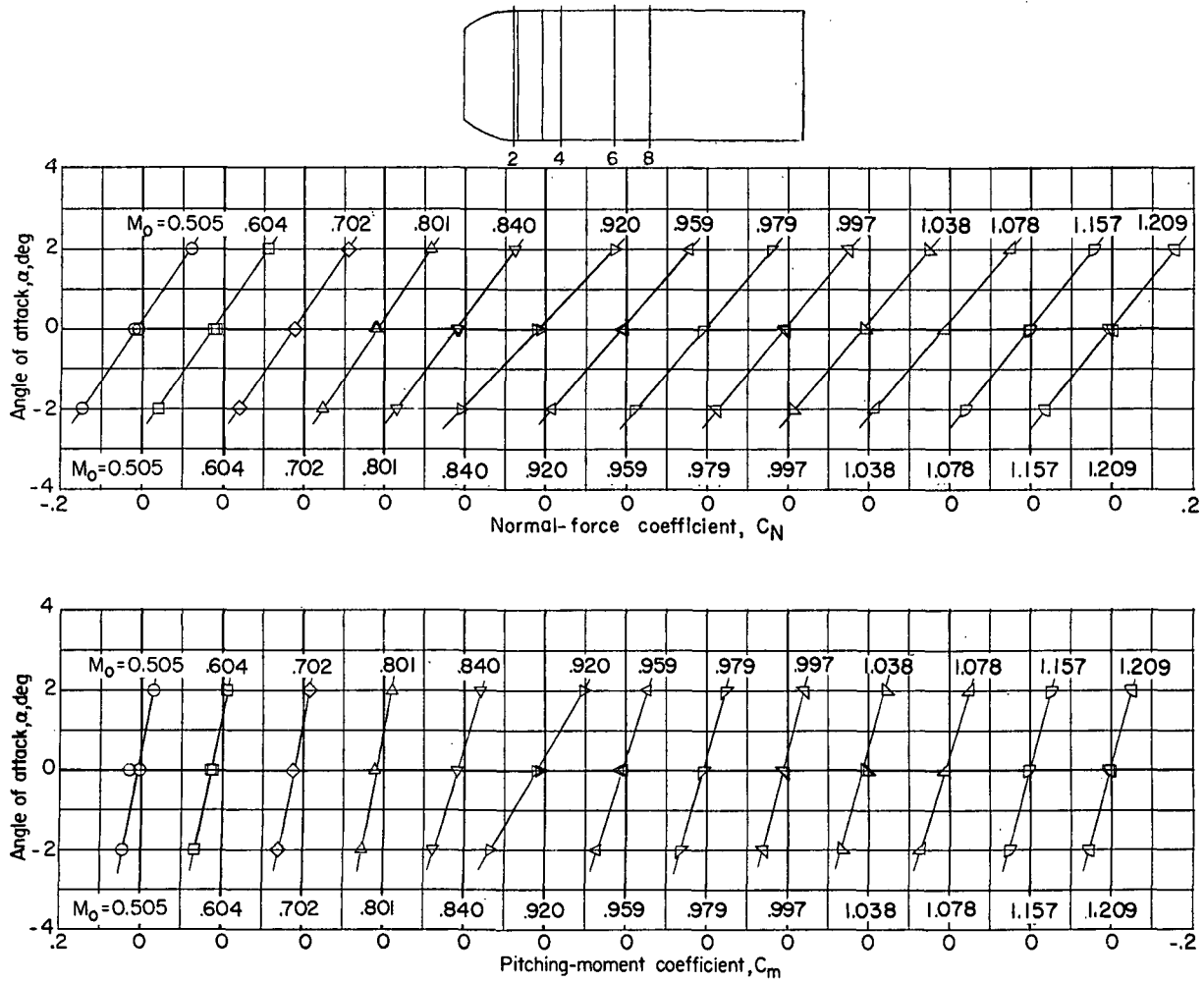


Figure 12.- The variation of normal-force and pitching-moment coefficients with angle of attack at different Mach numbers for the TX-21, nose B, configuration.

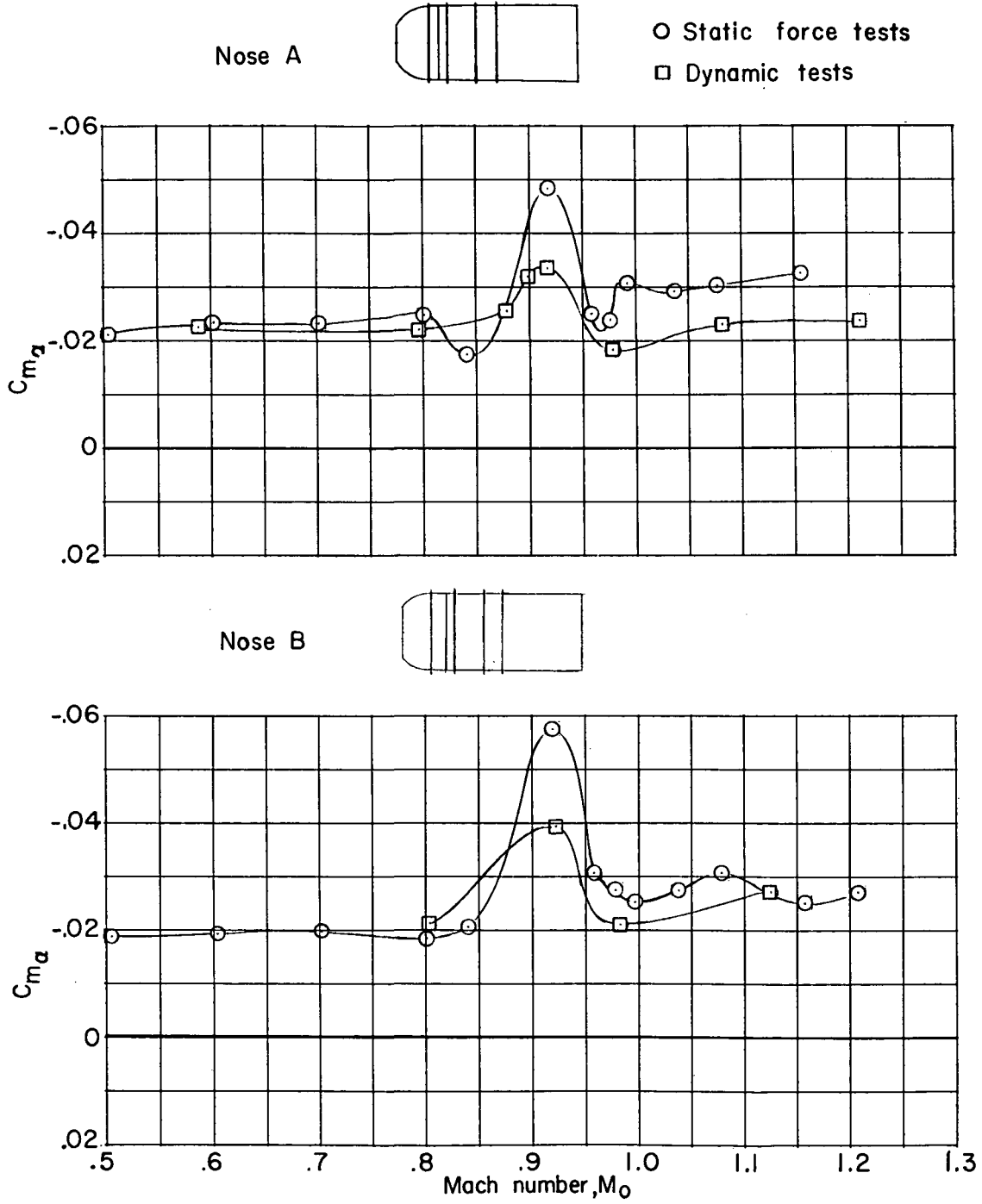


Figure 13.- Comparisons of the static stability parameter  $C_{m_\alpha}$  as obtained from static and dynamic tests of the TX-21 configurations.

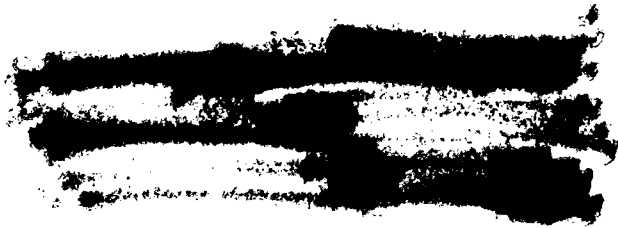


INDEX

<u>Subject</u>	<u>Number</u>
Bodies - Shape Variables	1.3.2
Stability, Longitudinal - Static	1.8.1.1.1
Loads, Aerodynamic	4.1.1
Loads, Aerodynamic - Tail	4.1.1.2

ABSTRACT

Tests were conducted in the Langley 8-foot transonic pressure tunnel to determine the afterbody pressure distribution and fin loading characteristics of two configurations of the TX-21 special weapon. The tests were conducted in the Mach number range from 0.50 to 1.21 at angles of attack from  $-2^\circ$  to  $+10^\circ$ . The Reynolds number variation was from  $1.05 \times 10^6$  to  $2.3 \times 10^6$ . Presented are the pressures over the model afterbody in the form  $p/p_0$  and loading characteristics of the stabilizing fins. Also presented are values of normal-force coefficient and pitching-moment coefficient for the complete configurations.



[REDACTED]

[REDACTED]

[REDACTED]